İSTANBUL TECHNICAL UNIVERSITY ★ INSTITUTE OF SCIENCE AND TECHNOLOGY

INTERFEROMETRIC FIBER OPTIC GYROSCOPE

M.Sc. Thesis by
İsmet Faik SAĞLAR, Eng.

Department : Electrical Engineering
Programme: Control and Automation Engineering

JUNE 2007

İSTANBUL TECHNICAL UNIVERSITY ★ INSTITUTE OF SCIENCE AND TECHNOLOGY

INTERFEROMETRIC FIBER OPTIC GYROSCOPE

M.Sc. Thesis by
İsmet Faik SAĞLAR, Eng.
504021137

Date of submission : 07 May 2007
Date of defence examination : 11 June 2007

Supervisor (Chairman) : Prof.Dr. Atilla BİR (İ.T.Ü.)

Members of the Examining Committee : Prof.Dr. Hakan TEMELTAŞ (İ.T.Ü)
Assis. Prof.Dr. B. Berk ÜSTÜNDAĞ (İ.T.Ü.)

JUNE 2007

İSTANBUL TEKNİK ÜNİVERSİTESİ ★ FEN BİLİMLERİ ENSTİTÜSÜ

İNTERFEROMETRİK FİBER OPTİK JİROSKOP

YÜKSEK LİSANS TEZİ

Müh. İsmet Faik SAĞLAR
504021137

Tezin Enstitüye Verildiği Tarih : 07 Mayıs 2007
Tezin Savunulduğu Tarih : 11 Haziran 2007

Tez Danışmanı : Prof.Dr. Atilla BİR (İ.T.Ü.)

Diğer Jüri Üyeleri : Prof.Dr. Hakan TEMELTAŞ (İ.T.Ü.)

Yrd.Doç.Dr. B. Berk ÜSTÜNDAĞ (İ.T.Ü.)

HAZİRAN 2007

ACKNOWLEDGEMENTS

I would like to acknowledge gratefully to my supervisor Prof. Dr. Atilla BİR for his guidance, support and encouragements during this thesis. I would also like to thank to Prof. Dr. Hakan TEMELTAŞ, Ast. Prof. Dr. Burak Berk ÜSTÜNDAĞ and Dr. Rıfat YENİDÜNYA for their guidance and support. I am also grateful to my friend Murat SEVEN for his help and suggestions. Finally, I would like to thank to my family for their patience, support and encouragements.

June 2007 **İsmet Faik SAĞLAR**

CONTENTS

ABBREVIATIONS

AC	: Alternating Current
AI	: Analog Input
APD	: Avalanche Photo Diode
AVAR	: Allan Variance
BFSL	: Best Fit Straight Line
CCW	: Counter Clockwise
CW	: Clockwise
DAC	: Digital to Analog Converter
DAQ	: Data Acquisition
DC	: Direct Current
DI	: Digital Input
EDFA	: Erbium Doped Fiber Amplifier
FOG	: Fiber Optic Gyroscope
GPS	: Global Positioning System
I-FOG	: Interferometric Fiber Optic Gyroscope
IMU	: Inertial Measurement Unit
INS	: Inertial Navigation System
LD	: Laser Diode
LED	: Light Emitting Diode
LIDAR	: Light Detection and Ranging or Laser Imaging Detection and Ranging
MonPD	: Monitor Photo Diode
PC	: Personal Computer
PCB	: Printed Circuit Board
PD	: Photo Detector / Photo Diode
PIN	: p-intrinsic-n
PIN PD	: p-intrinsic-n layered Photo Diode
PMF	: Polarization Maintaining/Preserving Fiber (Single Mode)
QEO	: Quadratic Electro-Optic
RT	: Rate Table
RLG	: Ring Laser Gyroscope
SLD	: Superluminescent Diode
SMF	: Single Mode Fiber
TIA	: Trans-Impedance Amplifier
UART	: Universal Asynchronous Receiver/Transmitter
UAV	: Unmanned Aerial Vehicle
UGV	: Unmanned Ground Vehicle
UUV	: Unmanned Underwater Vehicle

LIST OF TABLES

LIST OF FIGURES

LIST OF SYMBOLS

π	: 3.14159...
c	: Speed of light in vacuum as constant
r	: Radius of the beam guiding system
ℓ	: Circumference of the beam guiding system
ℓ_{CCW}	: Increased pathlength for counterclockwise rotating beam
$\Delta\ell_{CCW}$	: Pathlength difference for counterclockwise rotating beam
ℓ_{CW}	: Decreased pathlength for clockwise rotating beam
$\Delta\ell_{CW}$	: Pathlength difference for clockwise rotating beam
Ω	: Rotation rate of the beam guiding system
Ω_{π}	: Rotation rate of the beam guiding system corresponding to $\Delta\phi_S = \pi$
Ω_{in}	: Rotation rate value entered in the rate table control command which is sent to the rate table controller serially by PC via UART [deg/s]
Ω_{RT}	: Analog rotation rate output of the rate table from its controller [±10V]
Ω_{IFOG}	: Un-Normalized rotation rate of the prototype IFOG [deg/s]
Ω^{*}_{RT}	: Corrected/calibrated analog rotation rate output of the rate table
Ω^{*}_{IFOG}	: Normalized rotation rate of the prototype IFOG [deg/s]
v	: Tangential velocity of the beam guiding system
τ	: Transit time for light to cycle the beam guiding system, time constant for Allan Variance
τ_{CCW}	: Traveling time of the counter clockwise propagating beam to reach the exit
τ_{CW}	: Traveling time of the clockwise propagating beam to reach the exit
$\Delta\tau$	: Time difference of the counterpropagating wavetrains
$\Delta\ell$	: Pathlength difference for the counterpropagating beams
ω	: Angular frequency of ligthwave
f	: Frequency of ligthwave
$\Delta\phi_S$, $\Delta\phi_R$	: Rotation induced phase difference due to Sagnac effect
λ	: Wavelength of the ligthwave in vacuum
a	: Area of the beam guiding system
n	: Refractive index of the medium
c_{mCCW}	: Velocity of light propagating counter clockwise in medium
c_{mCW}	: Velocity of light propagating clockwise in medium
$\Delta\ell_{mCCW}$	: $\Delta\ell_{CCW}$ in medium with refractive index n
$\Delta\ell_{mCW}$	: $\Delta\ell_{CW}$ in medium with refractive index n
τ_{mCCW}	: τ_{CCW} in medium with refractive index n
τ_{mCW}	: τ_{CW} in medium with refractive index n
$\Delta\tau_m$	: $\Delta\tau$ in medium with refractive index n
$\Delta\ell_m$	: $\Delta\ell$ in medium with refractive index n
D	: Mean fiber coil diameter
L	: Total coil length of optical fiber
N	: Number of turns in optical fiber coil
A	: Total area enclosed by optical fiber coil

I	: Intensity of light at the photo detector
I_0	: Mean value of the intensity
ϕ_b	: Applied phase bias
$\Delta\phi_{FB}$	: Feedback bias to compensate the Sagnac phase shift
$\Delta\tau_g$	: Time to travel coil of light
f_m	: Modulation frequency
t	: Time
ϕ_m	: Phase modulation for biasing
$\Delta\phi_m$	: Phase difference of biasing modulation
f_p	: Proper or eigen frequency of the coil
V_{RT}	: Analog rotation rate output of the rate table [±10V]
V_{BIAS_RT}	: Static bias/offset on analog output of the rate table in Volts
V_{PD}	: Amplified analog output of the photo diode
V_{MonPD}	: Amplified analog output of the monitor photo diode
V_{BIAS_IFOG}	: Bias voltage of IFOG when there is no rotation
V_{IFOG}	: Un-Normalized analog voltage output of IFOG
V_{IFOG}^{*}	: Normalized and corrected analog voltage output of IFOG
SF_{RT}	: Scale factor of rate table [(deg/s)/Volt]
SF_{IFOG}, SF_E	: Electrical scale factor of the prototype IFOG [V/(deg/s)]
SF_O	: Optical scale factor of the prototype IFOG [rad/(rad/s)]
SF_{RT}^{*}	: Corrected scale factor of rate table [(deg/s)/Volt]

INTERFEROMETRIC FIBER OPTIC GYROSCOPE

SUMMARY

In this study, acquisition of principles of interferometric fiber optic gyroscope based on Sagnac effect, along with development and calibration of a prototype gyroscope is targeted. Although, first interferometric fiber optic gyroscope was developed in 1976, it was after 1990 for the fiber optic gyroscope to earn maturity and be used. Now, it is used as a primary inertial navigation sensor in land, air, sea and space applications. Another purpose of this work is to constitute know-how and basis for manufacturing of interferometric fiber optic gyroscope in our country. Components of the developed gyroscope were selected among easy supplied parts. In this way, component shortage will not be an issue and easy manufacturability is assured. According to sensitivity measurements performed, without appropriate measurement and calibration devices, minimum 0.05 degrees per second rotation rate was easily sensed by the fiber optic gyroscope which was constructed in laboratory. This sensitivity could be easily enhanced by application of proper packaging and calibration methods, to minimum 0.01 degrees per second which is suitable for short range tactical applications and robotic navigation systems.

In the first chapter, a short introduction about optical gyroscopes is given. In the second chapter, principles of fiber optic gyroscopes, configuration types and noise sources are mentioned about. In the third chapter, components of fiber optic gyroscopes is given with their properties and selection criteria. In the fourth chapter, all experimental work done during this thesis is explained and results are given. Construction of the developed fiber optic gyroscope, properties of chosen configuration and calibration process with detailed explanations accompanying plots are presented in this chapter. In the last chapter, evaluation of obtained results is given and discussed.

İNTERFEROMETRİK FİBER OPTİK JİROSKOP

ÖZET

Bu çalışmada, Sagnac etkisine dayanan interferometrik fiber optik jiroskopların çalışma prensiplerinin öğrenilmesi yanında bir adet prototip jiroskopun geliştirilmesi ve kalibrasyonunun yapılması amaçlanmıştır. İlk interferometrik fiber optik jiroskop 1976 yılında geliştirilmiş olmasına rağmen olgunluğa erişip kullanıma girmesi 1990'lı yılları bulmuştur. Şu anda kara, hava, deniz ve uzay uygulamalarında birincil ataletsel seyrüsefer sensörü olarak kullanılmaktadır. Yapılan çalışmanın amaçlarından bir diğeri de interferometrik fiber optik jiroskopun ülkemizde üretimi için bilgi birikimi ve altyapı oluşturmaktır. Geliştirilen jiroskopun kolay temin edilebilir komponentlerden oluşması tercih edilmiştir. Böylelikle, parça sıkıntısı çekilmeyecek ve kolay imal edilebilir olacaktır. Laboratuarda inşa edilen fiber optik jiroskobun, uygun ölçüm ve kalibrasyon cihazları olmadan, yapılan hassasiyet ölçümlerinde sensörün en az 0.05 derece/saniye'lik dönüş hızlarını sorunsuz algılayabildiği gözlemlenmiştir. Bu hassasiyetin uygun paketleme ve hassas kalibrasyon yöntemlerinin uygulanmasıyla en az 0.01 derece/saniye'ye ulaşacağı öngörülmüştür ki bu kısa menzilli taktik uygulamalar ile robotik seyrüsefer sistemleri için yeterli olmaktadır.

Birinci bölümde, kısaca optik jiroskoplar tanıtılmaktadır. İkinci bölümde, fiber optik jiroskoplara ilişkin temellerden, konfigürasyon çeşitlerinden ve hata kaynaklarından bahsedilmiştir. Üçüncü bölümde, fiber optik jiroskoplarda kullanılan optik komponentler hakkında bilgi verilmiş ve seçilen komponentlerin özellikleri ve seçim kriterleri anlatılmıştır. Dördüncü bölümde ise, tez sırasında yapılan tüm deneysel çalışma açıklanmış ve bunun sonuçları verilmiştir. Bu bölümde, geliştirilen interferometrik fiber optik jiroskobun inşaası, seçilen konfigürasyona ait özellikler, kalibrasyon aşamaları ile bunların detaylı grafiklerle sunumu yapılmıştır. Son bölümde ise, ulaşılan sonuçların değerlendirilmesi verilmiştir.

1. INTRODUCTION

The science of guidance, navigation, and control has been under development for over 100 years. Invention of gyroscope in 19th century measuring angular velocity, made it possible to develop inertial navigation systems (INS). Many exciting developments have taken place in that time, especially in the area of inertial navigation sensors. Today, to understand fully the entire range of navigation sensors, one needs to know a wide range of sciences such as mechanical engineering, electronics, control, electro-optics, optics and physics. Recently, the development and wide use of global positioning system (GPS) has enhanced the role of traditional navigation sensors, and is able to provide quick, inexpensive answers to the basic navigation questions of: (i) where did I start from and where do I want to go, and (ii) where is my position and what is my velocity now with respect to where I started. In fact, many navigation missions can be accomplished with GPS alone, with the inertial sensors used only for stabilization and control. However, the vulnerability of GPS to jamming means that inertial navigation sensors are still required, and also for applications where GPS is unavailable (such as indoors or in tunnels and caves), or cannot be acquired quickly enough (such as very short-time-of-flight munitions). The fact that an inertial (gyroscope or accelerometer) sensor's output drifts over time means that inertial navigation alone has an upper bound to mission accuracy. Therefore, in the absence of GPS, various augmentation sensors are also tied into the inertial systems; odometers, altimeters, gyrocompasses, star trackers, magnetometers, LIDAR, etc.

1.1 Background of Optical Gyroscopes

In 1913, French scientist Sagnac demonstrated that it is also possible to detect rotation with respect to inertial space with an optical system that has no moving parts. The effect is called after him. He used a ring interferometer and showed that rotation induces a phase difference between two counterpropagating paths. The original set-up was very far from a practical rotation rate sensor, because of its very limited sensitivity. In 1925, Michelson and Gale were able to measure earth rotation with a giant ring interferometer of almost 2 km in perimeter. The Sagnac effect is very small, so it was not possible to get usable performance from a reasonably compact device for any practical application at the times it was discovered [11].

One of the main advantages of the optical gyroscopes compared to its mechanical counterpart is the absence of rotating parts. This makes the optical gyro potentially longer lasting and robust.

1.1.1 Ring Laser Gyroscopes

Shortly after the invention of the laser in 1960, Rosenthal proposed to enhance the sensitivity with a ring laser cavity in 1962 where the counterpropagating waves recirculate many times along the closed resonant path instead of once like in the original Sagnac interferometer. And in 1963 this scheme was first demonstrated by Macek and Davis which is called ring laser gyroscope (RLG). Nowadays, RLG is used in many inertial navigation applications [10,11].

RLG uses mirrors like Sagnac's device. However, the loop is closed upon itself and no external source is used. A gas laser gain medium inside the loop gives rise to two counterpropagating laser beams in the loop. Figure 1.1 shows a typical RLG configuration. The basic Sagnac phase difference becomes converted to a frequency difference between these two beams, which can be measured with great simplicity and accuracy [10].

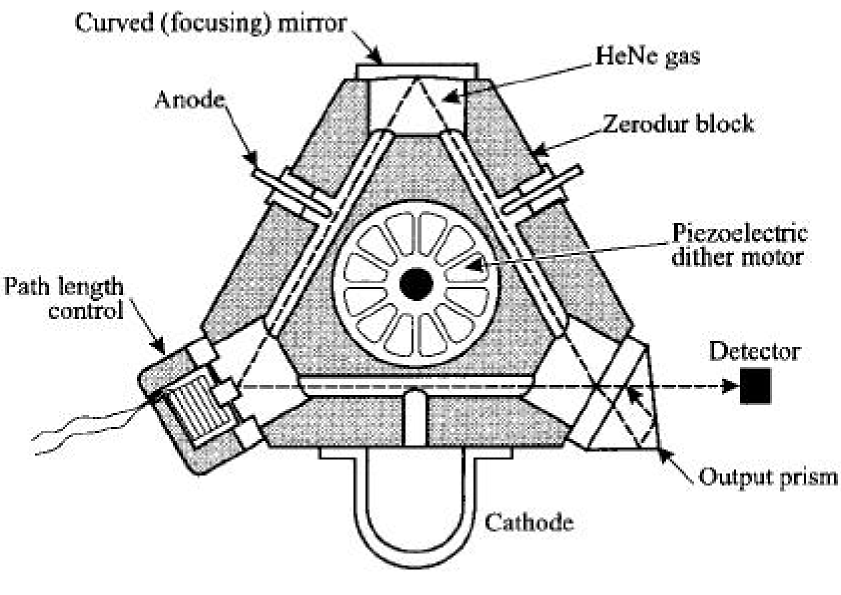

Figure 1.1: Ring Laser Gyroscope (RLG)

There is a problem with RLG which occurs by the backscatter from the mirrors causing the two counter-propagating waves to lock frequencies at very low input rates, known as lock-in. This can be overcome by introducing a frequency bias by means of a piezo-electric drive which dithers the RLG at several hundred hertz about its input axis. A real ring laser gyroscope is shown in figure 1.2.

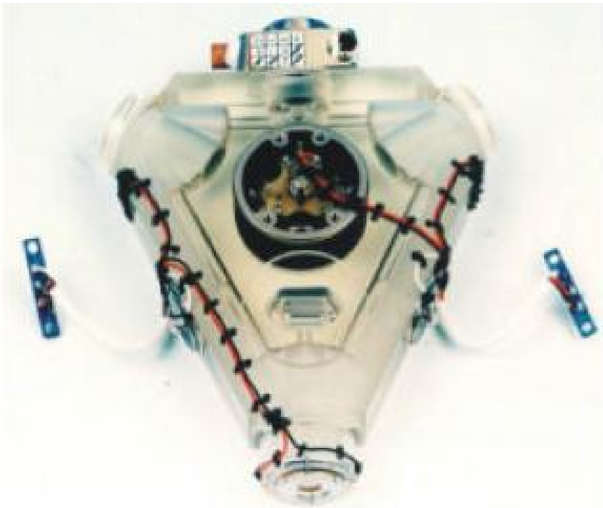

Figure 1.2: Real Ring Laser Gyroscope

1.1.2 Fiber Optic Gyroscopes

In 1970s when low-loss optical fiber, solid-state semiconductor light source and detector is introduced it became possible to use a multiturn optical fiber coil instead of a ring laser to enhance the Sagnac effect by multiple recirculation which was proposed in 1967 by Pircher and Hepner. But demonstrated experimentally later by Vali and Shorthill in 1976 with 950m long optical fiber coil.

Interferometric Fiber optic gyroscope (I-FOG) is a sensor that uses the interference of light to detect absolute mechanical rotation. I-FOG does not need to be in the center of rotation and it is also insensitive to linear motion. Thus, I-FOG is a true inertial sensor. A real fiber optic gyroscope is shown in figure 1.3.

FOGs are used in inertial navigation systems (INS), platform stabilization, inertial measurement systems (IMU) for aircraft, submarine and missiles, and as the guidance system for the Boeing 777. Other applications where fiber optic gyros are being used include mining operations, sewage pipe mapping, tunneling, attitude control of helicopters and stabilization of their camera & thermal imaging systems, cleaning robots, precision antenna pointing & tracking, turret stabilization and guidance for unmanned ground, aerial and underwater vehicles (UGV, UAV, UUV respectively). Even the rockets that carry Mars Explorers to Mars used FOG technology for navigation. An interesting application of FOGs include measurement of deformations of large-sized objects with the utilization of differential gyro technique. This is mainly used in torsion sensing & monitoring of ships and high buildings such as aircraft carriers and skyscrapers.

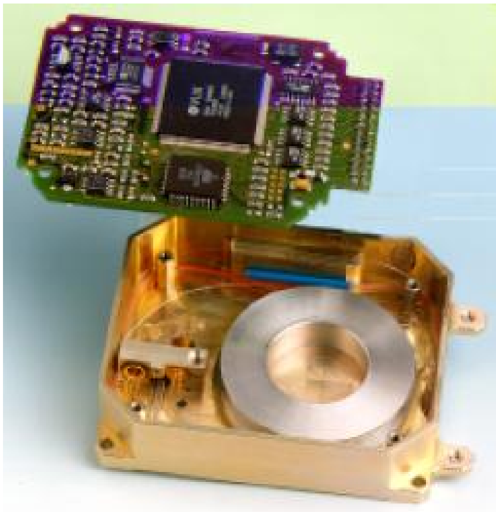

Figure 1.3: Real Fiber Optic Gyroscope

Advantages of FOG over RLG are;

- Solid State – No moving parts!
- Higher Resolution & Precision
- Adjustable Range & Resolution by Changing only Length of Fiber & Diameter of Loop (Loop Area)
- No Lock-In Problem
- Low Power Consumption – Low Voltage Operation
- Lightweight & Miniature Manufacturing
- High “G” Resistant – Launchable inside an ammunition
- Radiation Resistant
- Low Cost
- Easy Manufacturing

2. OVERVIEW OF FIBER OPTIC GYROSCOPES

2.1 Sagnac Effect

2.1.1 Description of Sagnac Effect [1,2,5]

The Sagnac effect is the relative phase shift between two beams of light that have traveled an identical path in opposite direction in a rotating frame.

A beam of light is split in two and the two beams are made to follow a ring trajectory in opposite directions enclosing an area. On return to the point of entry the light is allowed to exit the apparatus in such a way that an interference pattern is obtained. The position of the interference fringes is dependent on angular velocity of the setup. This arrangement is also called a Sagnac interferometer.

Sagnac effect is a pure relativistic effect where the traveling time difference of two counterpropagating signals using the same loop is measured.

2.1.2 Georges Sagnac [1,3,5]

Georges Sagnac (1869-1926) was a French physicist who lent his name to the Sagnac effect, a phenomenon which is at the basis of interferometers, laser gyroscopes and fiber optic gyroscopes developed since the 1970s. Little is known about the life of Georges Sagnac, other than that he was one of the first people in France to study X-rays, following Wilhelm Conrad Röntgen while he was still a lab assistant at the Sorbonne. In 1913, Georges Sagnac showed that if light is sent in two opposite circular directions on a revolving platform, the speed of the light beam turning in the same direction as the platform will be greater than the speed of the light beam that is turning opposite the direction of the table. The results of this experiment seemed to contradict the then-new theory of relativity. Georges Sagnac was an ardent opponent of the theory of relativity, but it was soon proven that the results could very well be explained by general relativity and later on special relativity. Figure 2.1 shows the original arrangement of Sagnac’s interferometer.

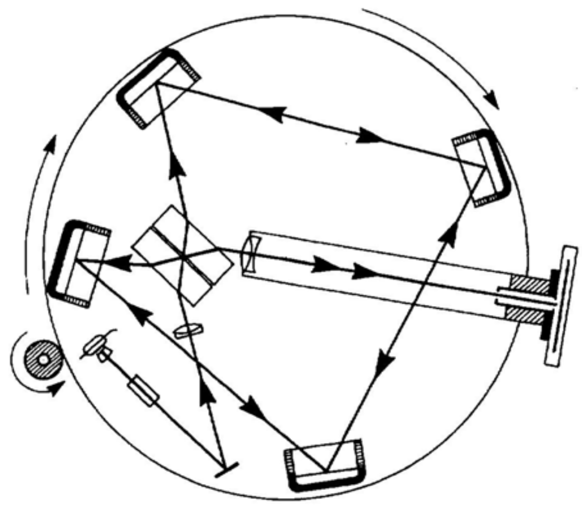

Figure 2.1: Sagnac Ring Interferometer Setup

Figure 2.2 shows the basic elements of a ring interferometer constructed with bulk optics: three mirrors and a beam-splitter. Two wavetrains, created by a beamsplitter, are traveling around the ring interferometer in opposite directions. If the beams after one turn are superposed they interfere and form a fringe pattern, which is made visible on a screen or received by a photo detector.

The light source, the beam guiding system (mirrors, prisms or glass fiber), combining optics, screen and/or photo detector are mounted on a platform. If the whole system rotates around an axis perpendicular to the plane of the counter propagating wavetrains, the fringe pattern will be shifted proportional to the rotation rate.

The actual effect is based on a traveling time or phase-difference between the two wavetrains. This leads to a shift of the interference fringe pattern, and this again can easily be detected.

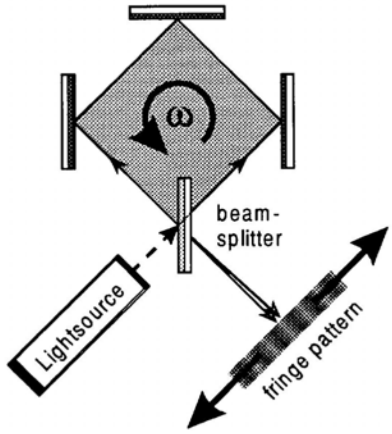

Figure 2.2: Basic Sagnac Ring Interferometer

2.1.3 Calculations in Vacuum [2, 4, 5]

Simple calculation of Sagnac effect based on circular wave guide configuration is given below. This wave guide, shown in Figure 2.3, is supposed to be in vacuum.

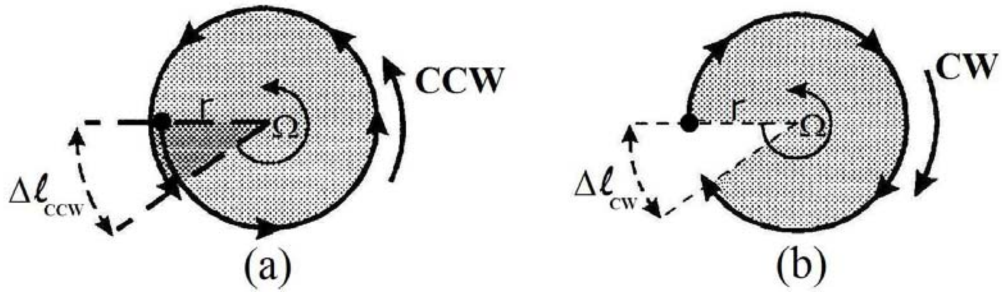

Figure 2.3: CCW and CW pathlengths induced by the Sagnac Effect

Light enters and exits the loop at a fixed point on the beam guiding system. If the beam guiding system rotates, the entry/exit point rotates with the beam guiding system. A time difference occurs for counter propagating light waves to complete one loop.

First consider light which is traveling counter clockwise (Figure 2.3a). For stationary situation the pathlength of the beam guiding system would be $\ell = 2\pi \cdot r$. But if the beam guiding system is rotating counterclockwise with angular velocity Ω, the pathlength increases to

$$\ell_{CCW} = \ell + \Delta\ell_{CCW} = 2\pi \cdot r + \Delta\ell_{CCW} \quad \textbf{(2.1a)}$$

And if it is rotating in clockwise direction, the path length decreases to

$$\ell_{CW} = \ell - \Delta\ell_{CW} = 2\pi \cdot r - \Delta\ell_{CW} \tag{2.1.b}$$

The counterclockwise and clockwise path length differences are calculated as $\Delta\ell_{CCW} = \Omega \cdot r \cdot \tau_{CCW}$, $\Delta\ell_{CW} = \Omega \cdot r \cdot \tau_{CW}$ where $v = \Omega \cdot r$ is the tangential velocity of the beam guiding system. C being the speed of light, the necessary traveling time of the counter clockwise propagating light wave to reach the exit point is calculated as

$$\tau_{CCW} = \frac{\ell + \Delta\ell_{CCW}}{c} = \frac{2\pi \cdot r + \Omega \cdot r \cdot \tau_{CCW}}{c} \tag{2.2}$$

Similarly the necessary traveling time of the clockwise propagating light wave to reach the exit point is calculated as

$$\tau_{CW} = \frac{\ell - \Delta\ell_{CW}}{c} = \frac{2\pi \cdot r - \Omega \cdot r \cdot \tau_{CW}}{c} \tag{2.3}$$

If equations (2.2) and (2.3) are arranged for τ_{CCW} counterclockwise and τ_{CW} clockwise traveling times, one obtain respectively

$$\tau_{CCW} = \frac{2\pi \cdot r}{c - \Omega \cdot r} = \frac{\ell}{c - v} \tag{2.4}$$

$$\tau_{CW} = \frac{2\pi \cdot r}{c + \Omega \cdot r} = \frac{\ell}{c + v} \tag{2.5}$$

The traveling time difference between these two wave trains is given as

$$\Delta\tau = \tau_{CCW} - \tau_{CW} = \frac{\ell}{c - v} - \frac{\ell}{c + v} = 2\pi \cdot r \cdot \left(\frac{2v}{c^2 - (v)^2} \right) = \frac{4\pi \cdot r \cdot v}{c^2 \cdot \left(1 - \left(\frac{v}{c} \right)^2 \right)} \tag{2.6}$$

Tangential velocity $v = \Omega \cdot r << c$ is rather small when compared with the speed of light c, so equation 2.4 for the $\Delta\tau$ traveling time difference simplifies to

$$\Delta\tau = \tau_{CCW} - \tau_{CW} \approx \frac{4\pi \cdot r \cdot v}{c^2} = \frac{4\pi \cdot r^2}{c^2} \cdot \Omega = \frac{4a}{c^2} \cdot \Omega = \frac{2r \cdot \ell}{c^2} \cdot \Omega \tag{2.7}$$

where $a = \pi \cdot r^2$ is the area enclosed by the beam guiding system. The $\Delta\ell$ path length difference is calculated as

$$\Delta\ell = \Delta\ell_{CCW} - \Delta\ell_{CW} = \Delta\tau \cdot c = \frac{4\pi \cdot r^2}{c} \cdot \Omega = \frac{4a}{c} \cdot \Omega = 2 \cdot \frac{v}{c} \cdot \ell \qquad \textbf{(2.8)}$$

The $\Delta\phi_S$ Sagnac phase shift is calculated as

$$\Delta\phi_S = \omega \cdot \Delta\tau = 2\pi \cdot f \cdot \Delta\tau = 2\pi \cdot \frac{c}{\lambda} \cdot \Delta\tau = \frac{8\pi^2 \cdot r^2}{\lambda \cdot c} \cdot \Omega = \frac{8\pi \cdot a}{\lambda \cdot c} \cdot \Omega = \frac{4\omega \cdot a}{c^2} \cdot \Omega \qquad \textbf{(2.9)}$$

where $\omega = 2\pi \cdot f$ is angular frequency and $f = \frac{c}{\lambda}$ is the frequency of light wave. Thus, as can be seen from equation 2.9, Sagnac phase shift is proportional to the a area of the loop, Ω rotation rate of the system and inversely proportional to the λ wavelength of the signal.

2.1.4 Calculations in Medium

In this section the Sagnac effect is calculated in the case of a dielectric wave guide with refractive index *n*. In a medium with refractive index *n* the velocity of light is calculated by relativistic considerations, which is different than the velocity in vacuum [8-12]. So the velocity of light propagating counter clockwise in medium is given as

$$c_{mCCW} \cong \tfrac{c}{n} + \Omega \cdot r \cdot \left(1 - \tfrac{1}{n^2}\right) \qquad \textbf{(2.10)}$$

Similarly the velocity of light propagating clockwise in medium is given as

$$c_{mCW} \cong \tfrac{c}{n} - \Omega \cdot r \cdot \left(1 - \tfrac{1}{n^2}\right) \qquad \textbf{(2.11)}$$

If in (2.2) and (2.3) we replace $\Delta\ell_{CCW}, \tau_{CCW}, c$ and $\Delta\ell_{CW}, \tau_{CW}, c$ with $\Delta\ell_{mCCW}, \tau_{mCCW}, c_{mCCW}$ and $\Delta\ell_{mCW}, \tau_{mCW}, c_{mCW}$, we obtain for τ_{mCCW} and τ_{mCW}, the propagation times respectively

$$\tau_{mCCW} = \frac{\ell + \Delta\ell_{mCCW}}{c_{mCCW}} = \frac{2\pi \cdot r + \Omega \cdot r \cdot \tau_{mCCW}}{c_{mCCW}} \qquad \textbf{(2.12)}$$

$$\tau_{mCW} = \frac{\ell - \Delta\ell_{mCW}}{c_{mCW}} = \frac{2\pi \cdot r - \Omega \cdot r \cdot \tau_{mCW}}{c_{mCW}} \tag{2.13}$$

If the equations (2.12) and (2.13) are solved for τ_{mCCW} and τ_{mCW}, the propagation times, can be written as

$$\tau_{mCCW} = \frac{2\pi \cdot r}{c_{mCCW} - \Omega \cdot r} = \frac{\ell}{c_{mCCW} - v} \tag{2.14}$$

$$\tau_{mCW} = \frac{2\pi \cdot r}{c_{mCW} + \Omega \cdot r} = \frac{\ell}{c_{mCW} + v} \tag{2.15}$$

respectively.

Thus, in a dielectric medium the traveling time difference between these two wave trains is obtained as

$$\Delta\tau_m = \tau_{mCCW} - \tau_{mCW} = \frac{\ell}{c_{mCCW} - v} - \frac{\ell}{c_{mCW} + v} = \frac{\ell \cdot \left[2v + \left(c_{mCW} - c_{mCCW}\right)\right]}{c_{mCCW} \cdot c_{mCW} + v \cdot c_{mCCW} - v \cdot c_{mCW} - v^2} \tag{2.16}$$

If equations (2.10) and (2.11) are applied in equation (2.16), $\Delta\tau_m$ traveling time difference is obtained as

$$\Delta\tau_m = \tau_{mCCW} - \tau_{mCW} \cong \frac{\ell \cdot \left(2r \cdot \Omega - 2r \cdot \Omega \cdot \left(1 - \frac{1}{n^2}\right)\right)}{\left(\frac{c}{n}\right)^2} = \frac{\ell \cdot \left(\frac{2r \cdot \Omega}{n^2}\right)}{\frac{c^2}{n^2}} = \frac{2r \cdot \ell}{c^2} \cdot \Omega \tag{2.17}$$

which is identical to the equation (2.7) in vacuum. Similarly, the path length difference $\Delta\ell_m$ is calculated as,

$$\Delta\ell_m = \Delta\ell_{mCCW} - \Delta\ell_{mCW} = \Delta\tau_m \cdot c = \frac{2r \cdot \ell \cdot \Omega}{c} = \frac{4\pi \cdot r^2}{c} \cdot \Omega = \frac{4a}{c} \cdot \Omega \tag{2.18}$$

which is identical with $\Delta\ell$ in vacuum as shown in equation (2.8). So Sagnac effect is not affected by the dielectric medium used as a waveguide.

2.1.5 Other Interesting Aspects related with Sagnac Effect

2.1.5.1 Effect of Linear Motion

Uniform velocity (translational motion) does not have any effect on Sagnac phase shift [5]. This feature gives the sensors based on Sagnac effect to sense absolute rotation.

2.1.5.2 Position of Center of Rotation

Sagnac phase shift is independent of the position of center of rotation. This is the most important feature of the Sagnac effect which makes it useful for inertial navigation [5,12].

2.1.5.3 Shape of Loop

Sagnac phase shift does not depend on the shape of optical fiber loop. So the shape of loop may be a square, rectangle or oval other than circle [12].

2.1.5.4 Velocity of Signal

Velocity of the signal does not change the Sagnac effect which also does not appear in any equations [5]. So using acoustic waves instead of light will not increase the sensitivity of the measurement system.

2.2 Fiber Optic Gyro Configurations

2.2.1 Principle of Reciprocity

An important factor in the Sagnac interferometer accuracy and performance is the reciprocity. An ideal fiber optic gyroscope should be able to measure only Sagnac phase shift. But to measure the Sagnac phase difference accurately, reducing of other phase differences which can vary under the influence of the environment is necessary. Success of this reduction determines the quality of the sensor. Thus, principle of reciprocity is incorporated for this purpose. [6]

In an ideal fiber optic gyroscope with reciprocal configuration, as shown in Figure 2.4, the counterpropagating optical waves that reach the photo detector are designed to travel exactly the same optical paths so that the rotation induced Sagnac phase shift is the only source of nonreciprocal phase shift [10]. Variations of the system by the environment, changes the phase of both waves equally so no difference in the phase delay results. In this way, the system obtains a basic degree of immunity to environmental influences that is probably beyond the capability of other phase stabilization techniques applied externally to the interferometer. [6]

2.2.2 Enhancement of Sagnac Effect with Fiber Optic Gyroscope

The advantage of using an optical-fiber coil to form the interferometer is that the Sagnac phase difference increases with the number of turns or the length of the fiber as shown in figure 2.4. Thus, fiber optic gyroscope is a multiplier of the Sagnac effect. Changing original Sagnac phase shift in equation (2.9) to;

$$\Delta\phi_S = \frac{8\pi \cdot N \cdot a}{\lambda \cdot c} \cdot \Omega = \frac{4\omega \cdot N \cdot a}{c^2} \cdot \Omega = \frac{8\pi \cdot A}{\lambda \cdot c} \cdot \Omega = \frac{4\omega \cdot A}{c^2} \cdot \Omega \qquad \textbf{(2.19)}$$

where A is total area of fiber loop which is N times a. Same equation may be written in terms of fiber length and diameter of the loop;

$$\Delta\phi_S = \frac{2\pi \cdot L \cdot D}{\lambda \cdot c} \cdot \Omega = \frac{\omega \cdot L \cdot D}{c^2} \cdot \Omega \qquad \textbf{(2.20)}$$

where D is the mean coil diameter, L is the total coil length equal to $\pi \cdot N \cdot D$ and Ω is the rotation rate component parallel to the coil axis.

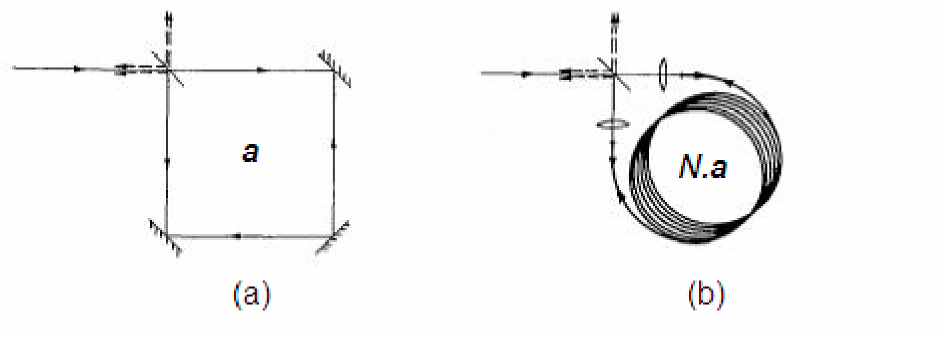

Figure 2.4: Enhancement of Sagnac Effect by FOG

From equation 2.20 we can derive, an important parameter of a fiber optic gyroscope: the optical scale factor, which is an indicator of sensitivity of the sensor;

$$SF_O = \frac{\Delta\phi_S}{\Omega} = \frac{2\pi \cdot L \cdot D}{\lambda \cdot c} = \frac{\omega \cdot L \cdot D}{c^2} \qquad \textbf{(2.21)}$$

Optical scale factor has the dimension of time which is in seconds.

2.2.3 Minimum Reciprocal Configuration

The commonly used minimum reciprocal configuration of fiber optic gyroscope describes an architecture with the minimum number of components capable of providing sufficient accuracy. A general block diagram of FOG of a minimum reciprocal configuration is shown in figure 2.5. Before invention of fiber couplers bulk optics were used to construct FOG configurations. Source splitter and coil splitters in figure 2.5 are beam splitter prisms and filter is optical fiber around 1 m in length used as a single mode filter to preserve reciprocity and provide a single path in the interferometer.

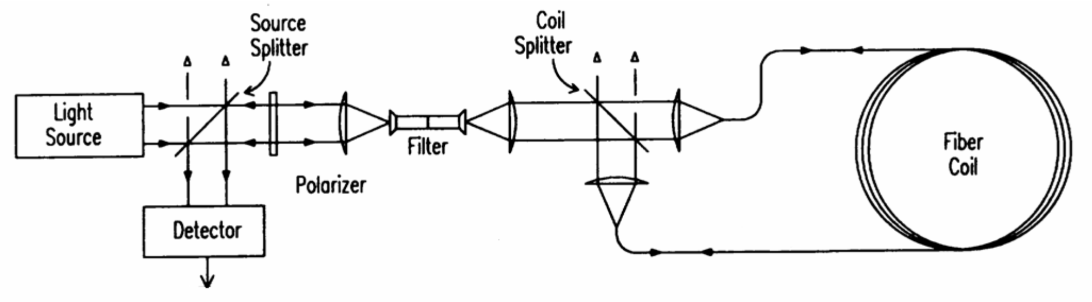

Figure 2.5: Minimum Reciprocal Configuration FOG

The output signal of a fiber gyroscope is the result of the interference of two waves as shown in equation (2.22) where I is intensity of light at the photo detector, I_0 is the mean value of the intensity, $\Delta\phi_S$ is the Sagnac phase shift. This response is called raised cosine as shown in figure 2.6 which has zero sensitivity around zero rotation rate due to result of the derivative $dI/d\Delta\phi_S$ being zero at $\Omega = 0$ corresponding to condition $\Delta\phi_S = 0$.

$$I = I_0[1 + \cos(\Delta\phi_S)] \quad \textbf{(2.22)}$$

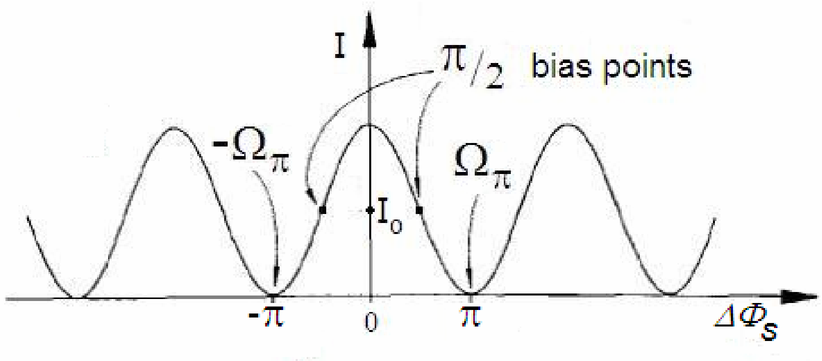

Figure 2.6: Output of Fiber Optic Gyroscope

2.2.4 Open Loop Configuration [11]

To maximize the scale factor of the sensor at low rotation rates, bias point of the minimum configuration FOG has to be shifted. Open loop configuration is developed to enhance sensitivity of FOG at zero rotation rate by the aid of a reciprocal phase modulator which is installed on one end of the fiber loop as shown in figure 2.7.

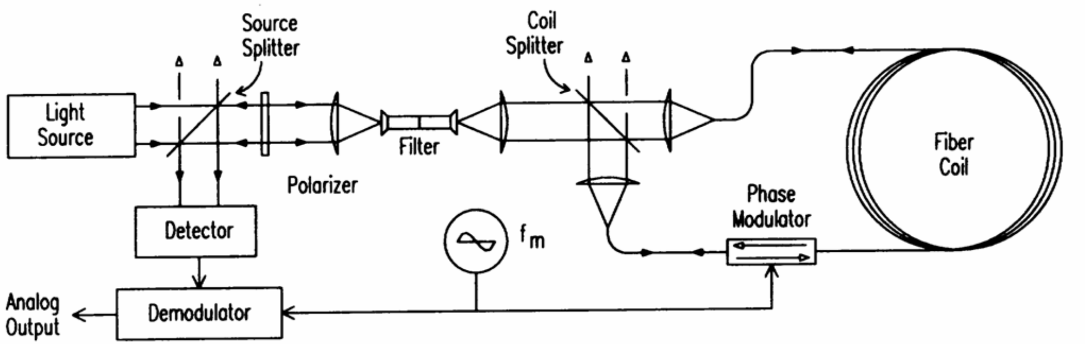

Figure 2.7: Open Loop FOG Configuration

To preserve reciprocity a reciprocal phase modulator is used. With bias applied the equation (2.22) changes to

$$I = I_0[1 + \cos(\Delta\phi_S + \phi_b)] \quad \textbf{(2.23)}$$

where I is intensity of light at the photo detector, I_0 is the mean value of the intensity, $\Delta\phi_S$ is the Sagnac phase shift and ϕ_b is the phase bias applied.

As shown in figure 2.8 the wave traveling in the clockwise direction is modulated when entering the coil and the counterclockwise propagating wave is modulated when leaving the coil. Thus, the counterpropagating waves turn out to be phase modulated with the same signal $\phi_m(t)$ but shifted in time $\Delta\tau_g$, which is equal to the difference between the time when the counterpropagating waves reach the modulator. Thus, the biasing modulation $\Delta\phi_m(t)$ of the phase difference is

$$\Delta\phi_m(t) = \phi_m(t) - \phi_m(t - \Delta\tau_g) \quad \textbf{(2.24)}$$

And the output intensity becomes

$$I = I_0[1 + \cos(\Delta\phi_S + \Delta\phi_m(t))] \quad \textbf{(2.25)}$$

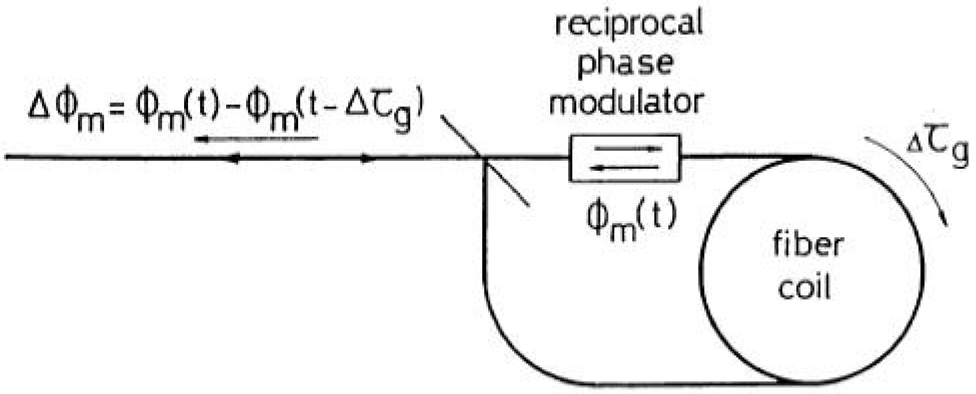

Figure 2.8: Introduction of Nonreciprocal Phase Shift with Reciprocal Phase Modulator

This phase modulation technique may be implemented with a square wave modulation $\phi_m(t) = \pm(\phi_b / 2)$ which yields a biasing modulation

$$\Delta\phi_m(t) = \pm\phi_b \tag{2.26}$$

Optimum bias points for maximum sensitivity are $\phi_b = \pm\pi/2$ which are shown in figure 2.6. Half period of the biasing modulation signal is $\Delta\tau_g$ which yields the frequency of the modulation as

$$f_p = 1/(2 \cdot \Delta\tau_g) \tag{2.27}$$

where f_p is called the proper or eigen frequency of the coil. This result may be interpreted as the proper frequency of a FOG. For silica fiber the proper frequency is given as

$$f_p = (100m \cdot MHz)/L \tag{2.28}$$

where L is total coil length of optical fiber.

Application of square wave phase bias is shown in figure 2.9. When FOG is at rest output is stable at a bias which is symmetric about the sinusoidal curve of output intensity. But, when the gyro is rotating, output swings around the bias point. Amplitude of this oscillation gives the rate of rotation. And the phase relation with input modulation gives the direction of the rotation.

In this configuration the nonlinearity of the intensity output, limits the performance and the dynamic range. So, another approach is used to solve these problems, which is called the closed loop configuration.

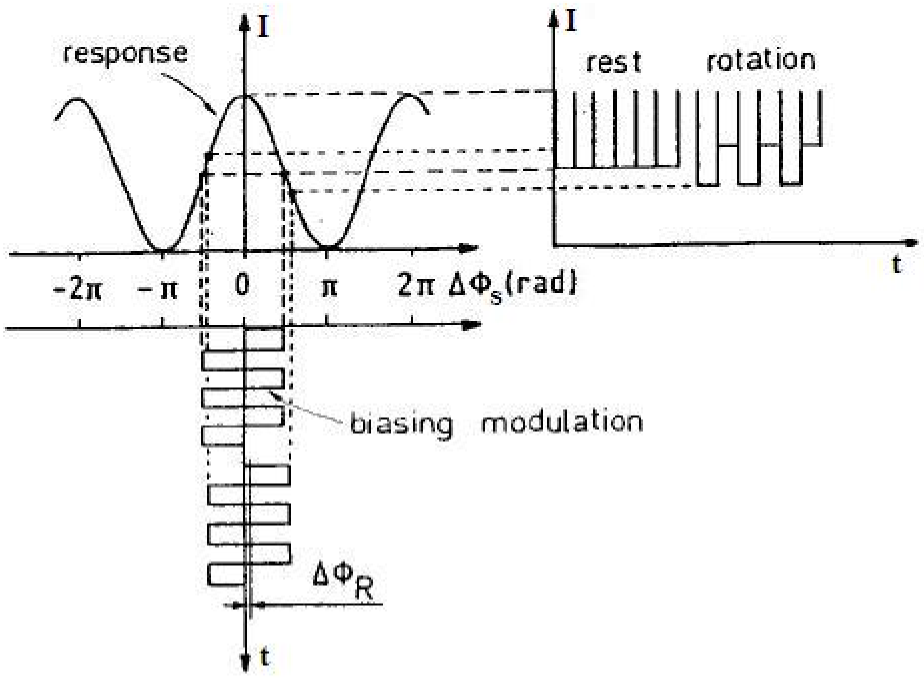

Figure 2.9: Square Wave Phase Modulation of Counterpropagating Waves in FOG

2.2.5 Closed Loop Configuration

In a closed-loop gyroscope a negative feedback mechanism maintains the open-loop signal at zero by compensating the Sagnac phase shift by introducing an equal and opposite phase shift within the sensing loop. This is shown in figure 2.10.

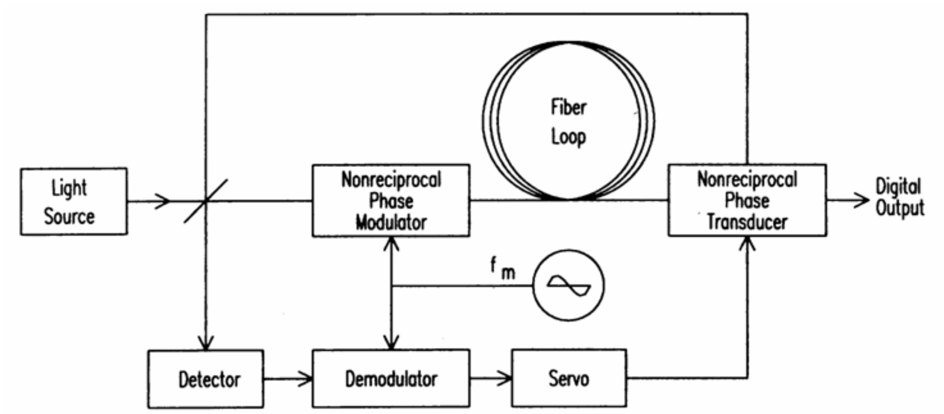

Figure 2.10: Closed Loop FOG Configuration

The measure of this added phase shift reveals the rotation-rate information as shown in figure 2.11.

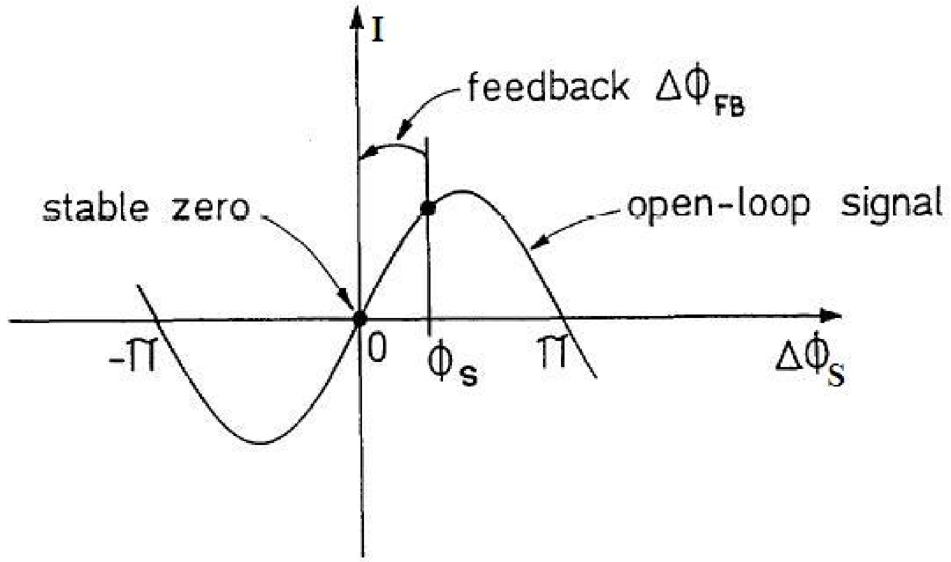

Figure 2.11: Principle of Closed-Loop Operation of FOG

2.2.6 Multi-Axis Architectures

To reduce component count, several multi-axis fiber optic gyroscope architectures are developed, which is shown in figure 2.12.

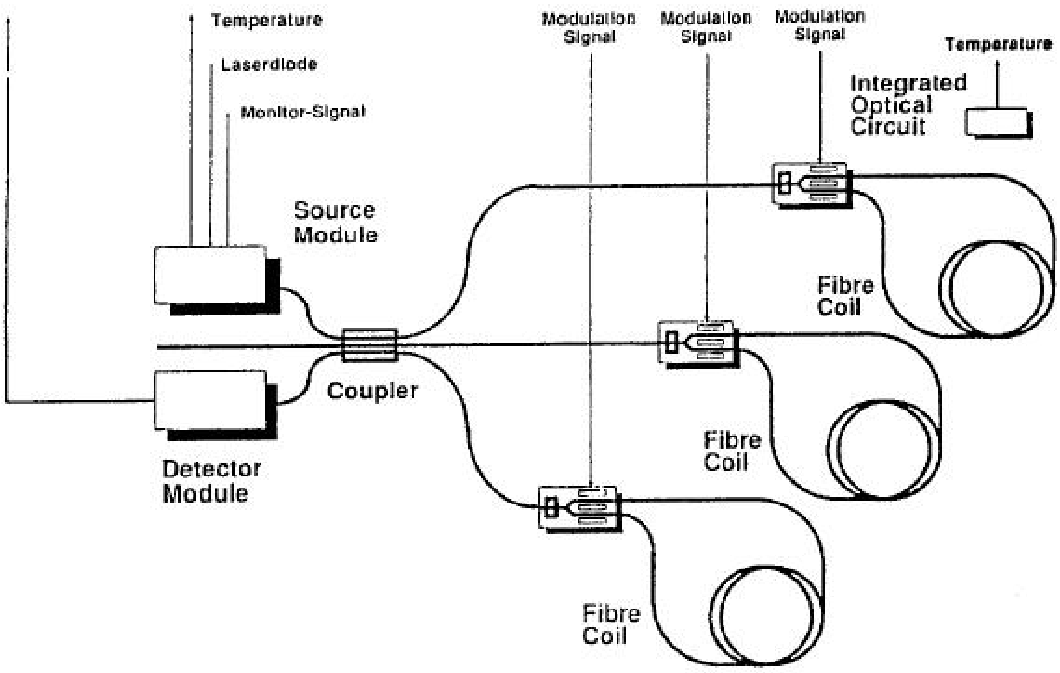

Figure 2.12: Source and Detector Sharing with Multi-Axis FOG Architecture

2.3 Fiber Optic Gyro Error Sources

In fiber optic gyroscope, a variety of non-reciprocal parasitic effects, comparable to or greater than the Sagnac phase difference, can create phase differences which degrade the performance of the sensor.

2.3.1 Faraday Effect

Faraday effect in fiber optic gyroscopes is a magnetically induced rotation of the optical polarization in fiber loop which is placed in a magnetic field gradient which is shown in figure 2.13. This effect is not distinguishable from Sagnac phase shift at the output detector. This often appears as a drift in the rotation rate. Numerically, the error due to the earth's magnetic field is typically 10 deg/h. [6,13,14]

In any interferometer it is necessary that the two beams possess identical states of polarization when they are superimposed on the detector. This condition is called full contrast. When interfering waves' state of polarizations match only partially, the contrast of interference is reduced. Also, if their state of polarizations are orthogonal, no interference occurs [10]. Faraday effect introduces a rotation of the optical polarization, which changes the state of polarization, causing reduction of contrast in turn.

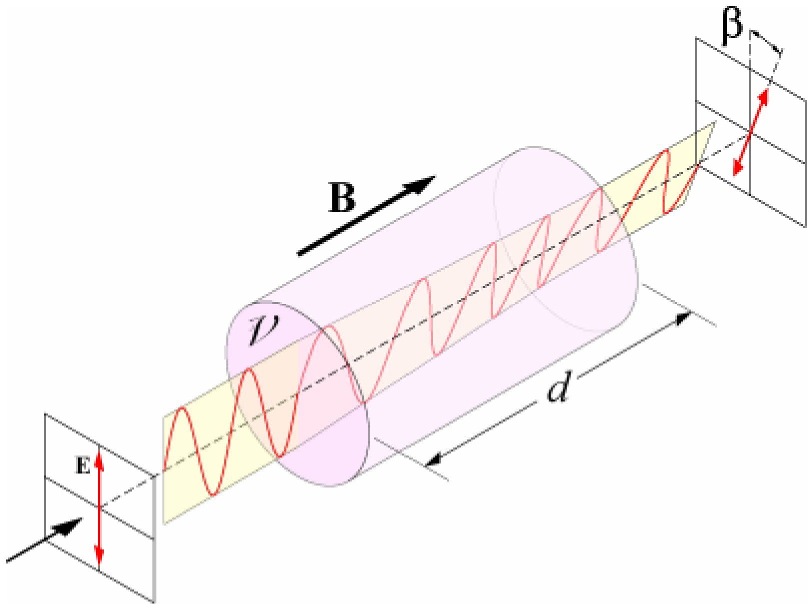

Figure 2.13: Faraday Effect [17]

Normally in a closed loop, the net Faraday effect should be zero. But, due to residual birefringence along the fiber, same state of polarization can not be preserved, which causes a Faraday phase shift accumulation. The influence of earth's magnetic field may also cause significant errors, unless required precautions are taken. [11]

There are many methods to reduce this effect. Some of them are; magnetic shielding, use of polarization preserving optical fiber and active control of state of polarization in fiber which are applied individually or all together. Also, use of longer wavelengths reduces Faraday effect by a factor of 3 to 4, due to the λ^{-2} dependence. Another approach to reduce Faraday effect in fiber optic gyroscopes, is the use of a depolarizer in single mode configuration. [11]

2.3.2 Kerr Effect

The Kerr Effect or the quadratic electro-optic effect (QEO effect), which was discovered in 1875 by John Kerr – a Scottish physicist, is a change in the refractive index of a material in response to an electric field. The Kerr-induced refractive index change is directly proportional to the square of the electric field. There are two special cases of the Kerr Effect: 1) the Kerr electro-optic effect (DC Kerr effect), 2) the optical Kerr effect (AC Kerr effect). [18]

The Kerr electro-optic effect is the special case, in which a slowly varying external electric field applied, for instance, by a voltage on electrodes across the material. Under the influence of the applied field, the material becomes birefringent, with different indexes of refraction for light polarized parallel or perpendicular to the applied field.

The optical Kerr Effect is the case in which, the electric field of the light propagating inside the material changes the refractive index of the material. This causes a variation in index of refraction which is proportional to the local intensity of the light.

The optical Kerr Effect in optical fibers is an optical-intensity-induced nonreciprocity. At high optical intensities, the propagation constants for the counterpropagating waves become intensity dependent. This is a nonlinear optical effect related to four-wave mixing that has found application in nonlinear spectroscopy. In particular, when the counterpropagating waves have unequal intensities, the propagation constants become unequal and cause a nonreciprocal phase shift indistinguishable from the Sagnac Effect. This effect could be minimized by the use of broadband light sources such as superluminescent diode with a broad frequency spectrum. When the Kerr Effect induced phase shifts are summed over the wavelength components of a broadband source, induced phase shift averages to zero. [13]

It may also be avoided by carefully balancing the splitting ratio of the main coupler of the gyro. [10]

2.3.3 Thermal Effects

Temperature changes and inequalities within fiber coil of the gyro induces significant phase errors which limits the sensitivity of the sensor. Thermally induced nonreciprocity may occur if there is a time-dependent temperature gradient along the fiber. Nonreciprocity arises when counterpropagating waves traverse the same region of the optical fiber at different times having different thermal states. If optical fiber's propagation constant varies at different rates along the fiber, the corresponding wave fronts in the two counterpropagating waves traverse a slightly different effective path. This in turn creates a relatively large nonreciprocal phase shift in a long fiber loop that is indistinguishable from the phase shift caused by rotation. [19]

Numerically, for a navigation grade fiber optic gyroscope the temperature should be controlled in the order of 10^{-3} °C which is very difficult to realize and maintain. So to reduce the effect, other methods are sought. One method is to use a fiber which has low refractive-index temperature coefficient. A second method is to wind the fiber coil so that parts of the fiber that are equal distances from the coil center are beside each other.

To reduce thermal effects two well-known winding methodologies are developed. These are called bipolar and quadrupolar winding. In both winding methods, fiber coil is wound from the middle by alternating layers coming from each half-coils. As shown in Figure 2.14, the only difference between bipolar and quadrupolar winding is the number of layers coming from each half-coils. [11]

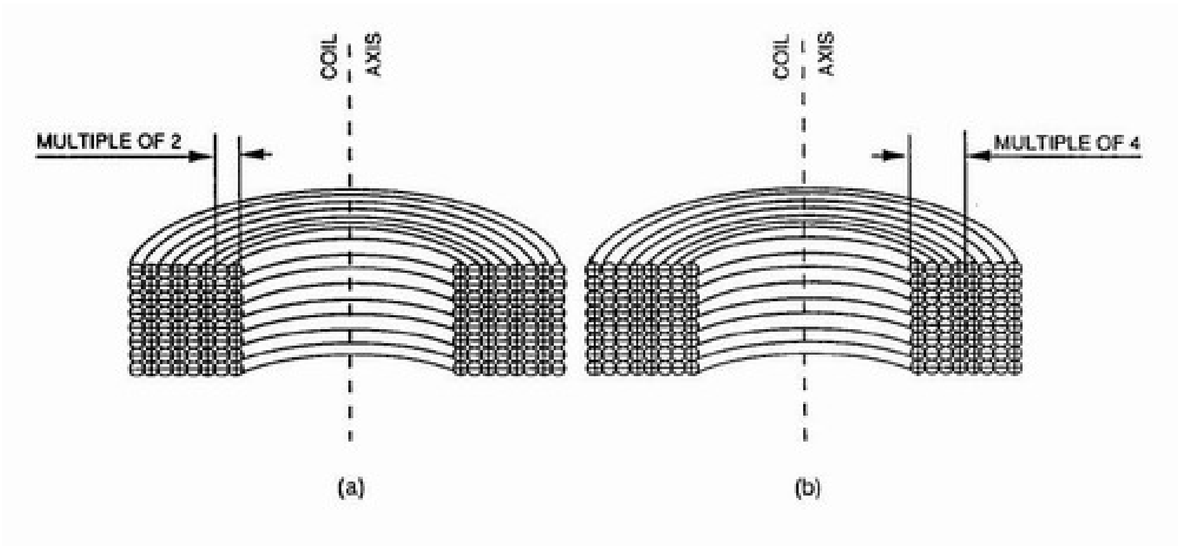

Figure 2.14: Cross-section of bipolar (a) and quadrupolar (b) windings

3. OPTIC COMPONENTS: PROPERTIES AND SELECTION

3.1 Light Sources

There are several types of light sources which can be used in FOG. Main types are explained below. All light sources which are going to be used in a fiber optic gyroscope should be fiber pigtailed, which eases coupling of light into fiber core and increases the efficiency. Some of these light sources have built-in monitor photo diode, which may be used as an optical feedback sensor for intensity control or a means of compensation for intensity changes.

3.1.1 Laser Diode (LD)

Laser diode outputs narrow bandwidth (near monochromatic), high intensity, coherent light. But these properties cause Kerr Effect and Rayleigh Backscattering problems which are explained in section 2.3. These light sources are also very expensive and require precise current and temperature control, which also increases cost of the sensor.

LDs are highly polarized light sources. This property requires alignment control of polarizers in the fiber optic system in order to retain much of the power in the system.

3.1.2 Light Emitting Diode (LED)

Light emitting diodes output broadband, very low coherent, low intensity light. Low efficiency of these light sources makes them unsuitable for fiber applications.

3.1.3 Superluminescent Diode (SLD)

Superluminescent diodes have similar manufacturing processes as laser diodes, but lasing is prevented. These types of light sources output broadband, low coherent and high intensity light, which does not cause Kerr Effect and Rayleigh Backscattering problems. Disadvantage of SLD is having poor wavelength stability, which requires precise current and temperature control.

3.1.4 Erbium Doped Fiber Amplifier (EDFA)

These light sources are manufactured using rare-earth doped fibers. These sources are superior to SLDs with their excellent wavelength stability and broader spectrum. EDFAs output unpolarized light which reduces polarization based errors. Disadvantages of EDFAs are high coherence, complex configuration and high cost.

3.2 Photo Detectors

Photo detectors convert intensity of light to electric current. Detector used in an interferometer application must have high quantum efficiency, high linearity, low noise and low temperature dependency.

3.2.1 PIN Photo Diode (PIN PD)

PIN photo diodes are high sensitivity, fast response and low noise detectors. Their gain is not high as APDs but their noise is much lower than APDs.

3.2.2 Avalanche Photo Diode (APD)

Avalanche photo diodes have high gain, but this gain is highly temperature dependant. They also have high noise and require a very high bias voltage.

3.3 Optical Fiber Couplers

There are many types of optical fiber couplers. Fused couplers are the most used types in fiber optic systems due to their low loss and easy connection. Function of coupler in fiber optic gyroscope is to split the light into two beams and recombine the split light beams to generate interference whose intensity is detected by the photo detector.

3.4 Polarizers and Polarization Controllers

Polarizers act like a filter of unwanted state of polarization. They only pass right aligned light whose state of polarization match with polarizer's. They are used to ensure reciprocity as explained in section 2.2.

3.5 Phase Modulators

There are several types of phase modulators: Piezoelectric Phase Modulator, Electro-Optic Phase Modulator, Acusto-Optic Phase Modulator.

3.5.1 Piezoelectric Phase Modulator

These types of modulators use the principle of contraction and expansion of piezocrystals as a result of the applied voltage. This property is used to change the length of the fiber, which is wound around a tube shaped piezocrystal, by applying the required voltage. This causes a pathlength change for the light traveling inside the fiber. Pathlength change can be adjusted by winding, tube geometry, piezocrystal properties and amplitude of drive voltage. Disadvantages of piezoelectric phase modulators are low bandwidth (frequency up to around 100 kHz) and requirement of very high drive voltages (~100V).

3.5.2 Electro-Optic Phase Modulator

Special dielectric waveguides, whose characteristics could be changed by applied electric field, are used to manufacture electro-optic phase modulators. Waveguide is placed between two electrodes which create the electric field by the application of drive voltage. Index of refraction is changed proportional to the drive voltage, which changes the propagation constant changing the pathlength of light.

3.6 Optical Fiber and Coil

Types of optical fiber that are used in a fiber optic gyroscope should have low loss, be highly linear and single-mode. According to system configuration polarization preserving optical fibers could also be used.

Fiber coil is the sensing element of fiber optic gyroscopes. Thus, it should be carefully wound to minimize thermal and stress gradients and asymmetries. Some of the winding techniques are explained in section 2.3.3.

Geometric properties of fiber coil, changes the sensitivity and the dynamic range of the gyroscopic sensor.

3.7 Selection of Optical Components

3.7.1 Optical Fiber

The optical fiber selected for the sensing coil is standard single mode fiber (SMF) which is vastly used in the telecommunication industry. This type of fiber is much cheaper than the polarization maintaining fiber (PMF). SMF is also produced by many manufacturers spread world-wide.

3.7.2 Light Source

Optoelectronic components of IFOG are selected with performance and cost considerations in mind. SLD with 1310 nm central wavelength was selected as the light source. This type of light source was selected firstly because broadband light sources prevent backscattering problems. Secondly, to use standard telecommunication fibers, the central wavelength of the light source should be 1310 or 1550 nm. At 1550 nm wavelength, loss in optical fiber is minimal. But, light sources with 1550 nm central wavelength are much more expensive than light sources with 1310 nm central wavelength. The selected SLD also has a built-in monitor photo diode (MonPD), which may be used for optical feedback to stabilize the intensity its output. However, in our IFOG, to reduce electronics, monitor photo diode's output is used in order to normalize the photo diode's output signal in case of varying SLD intensity. Normalization is done by digital signal processing which is cheaper than designing and building extra electronic circuits, which also consumes board space. Temperature control of SLD is very important which affects the stability of central wavelength. SLD used in our IFOG does not have a built-in thermo-electric cooler (TEC), which is normally used for temperature stabilization of the SLD. Built-in TEC, doubles the cost of the SLD unit and increases power consumption.

3.7.3 Photo Detector

PIN type photo detectors are selected for their fast response, high sensitivity and low noise, which make them ideal detectors for fiber optic gyroscopes.

3.7.4 Couplers

Wideband fused couplers are selected for their low insertion loss and accurate splitting performance.

4. EXPERIMENTAL WORK AND RESULTS

4.1 Fusion Splice and Construction of IFOG

Fiber optic gyroscope, designed in this thesis, is constructed with a low loss and accurate method called fusion splicing. This is a complex method to fuse two optical fibers together by melting and welding by an accurately timed electrical arc as shown in figure 4.1.

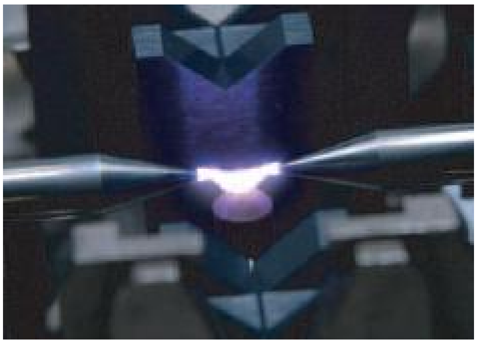

Figure 4.1: Arc generated by a fusion splicer

This method requires the use of specialized precision machines. Fusion splicing is divided into two phases: preparation and splicing. First, the coating of optical fiber is stripped. Then, the fiber end is cleaned from micro glass particles and dust by ultrasonic cleaning. After that, end of optical fiber is cleaved (chopped) by means of a diamond blade with a maximum 1 degree error. This process is repeated for the other end of fiber.

When two ends are prepared for fusion splicing they are placed in the fusion splicer machine and according to the properties of fibers being spliced, an appropriate splicing program is selected. If necessary, any required changes are adjusted using the menu of the device. Then the fusion splice process is started.

Fusion splicer first aligns the optical fiber ends in three axes as shown in figure 4.2, 4.3a and inspects them via optical cameras by the help of image processing techniques.

Figure 4.2: Alignment of fiber ends in three axes

Then calculates required arc duration and power and applies the arc. Finally two fiber ends became spliced together with approximately 0.02dB loss. Spliced fiber ends are shown in figure 4.3b. Sometimes errors may happen in fusion splicing: misalignment as shown in figure 4.3c, or cladding over melt due to excess arc power and/or duration as shown in figure 4.3d.

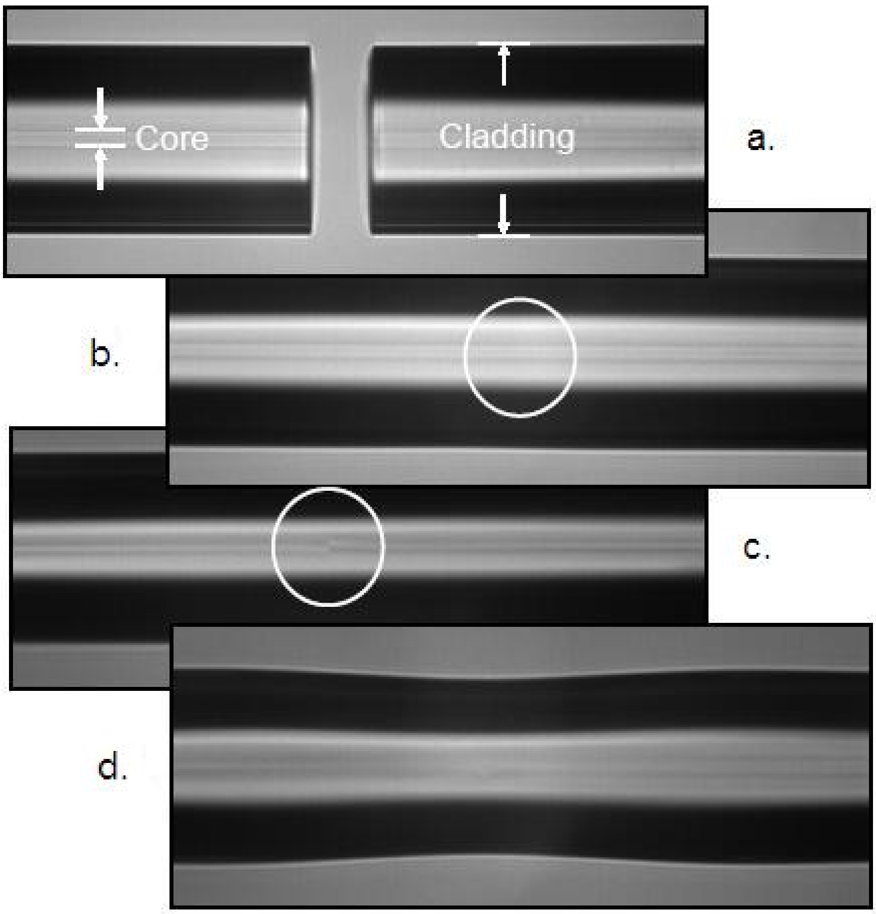

Figure 4.3: Fusion Splice a. alignment, b. good splice, c. misalignment, d. excess arc

This process is repeated for all joints. Figure 4.4 shows a picture of the construction process of IFOG#1 in progress.

Figure 4.4: Construction of IFOG#1

In figure 4.5 oscilloscope output is shown while the IFOG is at rest. Channel 1 is the signal of the output detector and channel 2 is the signal of monitor photo diode which monitors the output intensity of the light source. As can be seen from the scope output, the intensity is much lower at the output detector of the IFOG.

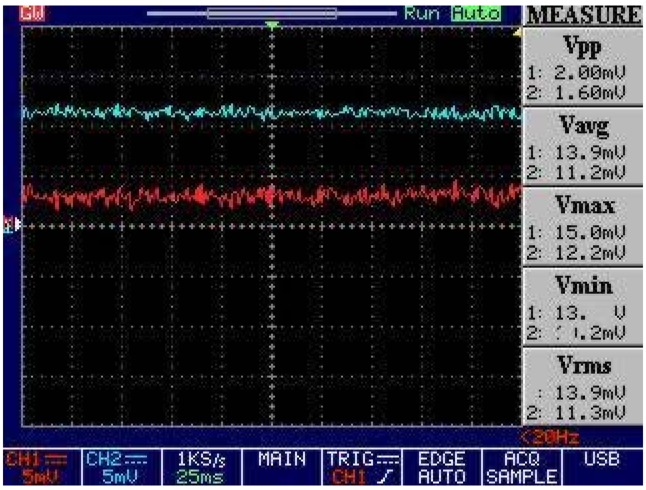

Figure 4.5: IFOG at rest

Figure 4.6 shows the scope output while the IFOG is rotated manually on a non-motorized rate table with a nearly sinusoidal rotation rate. Then after these preliminary tests, IFOG has to be calibrated in order to obtain its performance parameters.

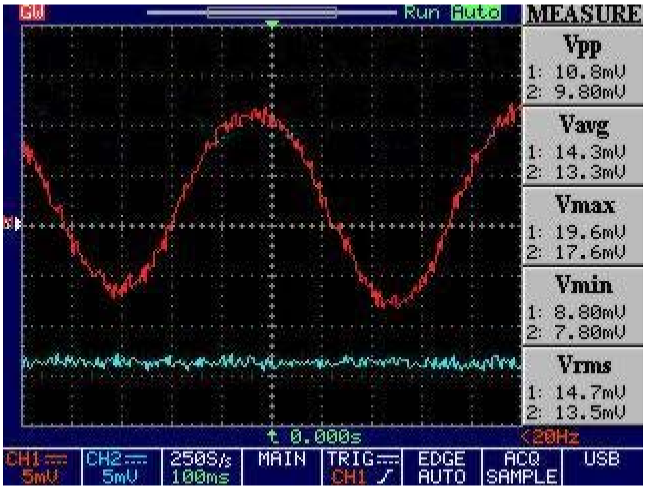

Figure 4.6: IFOG experiencing sinusoidal rotation

4.2 Configuration and Properties of the IFOG Prototypes

Construction parameters of the developed IFOG prototypes are shown in table 4.1. Sensitivity of IFOG, optical scale factor SF_O, is calculated according to the given parameters with equation 2.21.

Table 4.1: Properties of the Interferometric Fiber Optic Gyroscope

Property	**Value**
Coil Length (L)	500 m nominal
Diameter (D)	3.5 inches nominal (~0.089 m)
Wavelength (λ)	1310 nm
Optical Scale Factor (SF_O)	0.71 s

Open-loop configuration is selected for the IFOG because of its simplicity and applicability. Block diagram of the IFOG with its electronics is shown in figure 4.7.

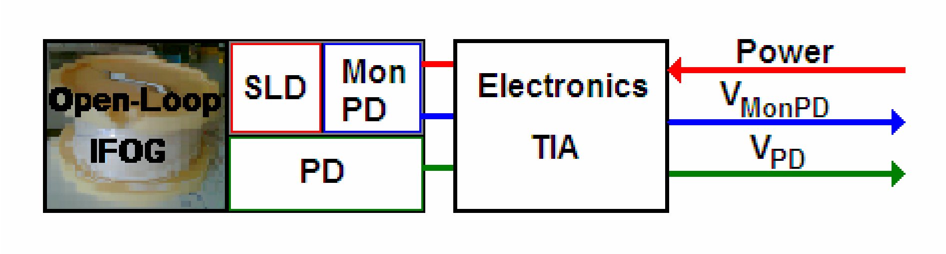

Figure 4.7: Configuration and block diagram of the IFOG

PD and MonPD output currents in 1-10 µA range. These currents are amplified and converted to Volts with the help of developed trans-impedance amplifier, TIA. Developed circuit incorporates both SLD drive electronics and TIAs. Circuit is built as PCB which also has connectors and cabling for proper connection to the data acquisition system.

Both prototypes, IFOG#1 and IFOG#2, do not have any shielding and temperature stabilization against environmental effects as shown in figure 4.8. IFOG#1 is the first built prototype, which is built on a platform. On the other hand, IFOG#2 is near ready for packaging, since it is built around a specially designed spool.

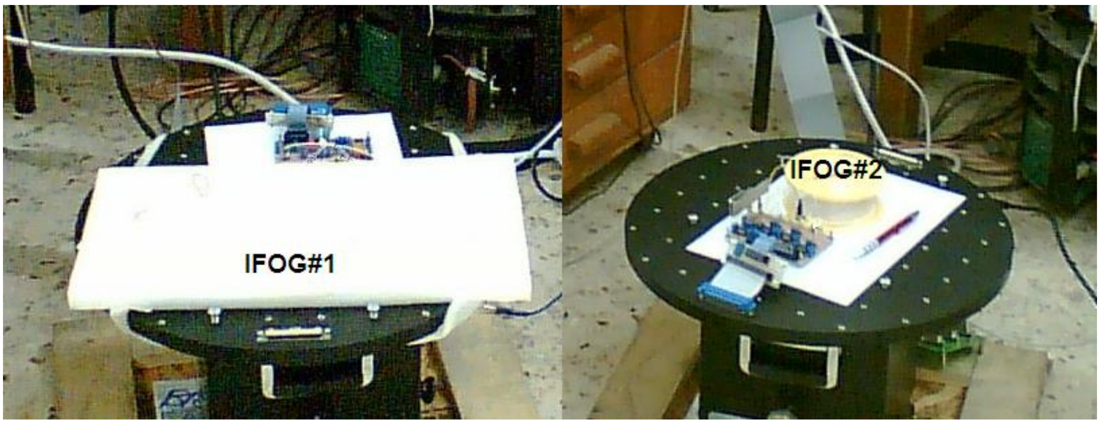

Figure 4.8: Built IFOG prototypes on the rate table

4.3 Calibration Procedure

Calibration of gyroscopes is done by using a rate table whose rate of rotation is controlled with high resolution and accuracy. Figure 4.9a shows a servo controlled rate table. During the calibration of gyroscopes, sensing axis of gyroscope should be orthogonal with the Earth's axis of rotation. Thus, the rotation of earth is not sensed by the gyroscope under calibration. This could be accomplished by means of a tilt stand mounted rate table as shown in figure 4.9b.

Figure 4.9: Rate table (a), with tilt stand (b)

Rotation rate component of the earth near our faculty building is calculated to be 9.89 deg/h with equation 4.1 as depicted in figure 4.10. [20,21]

$$\Omega_{E\_IFOG} = \sin(latitute = \alpha) \cdot \Omega_E = \sin(41.10483°) \cdot 15.04106° / h \cong 9.89° / h \qquad \textbf{(4.1)}$$

This rotation rate is well below our expected noise and resolution. So the prototype IFOGs are not tilted during the calibration process.

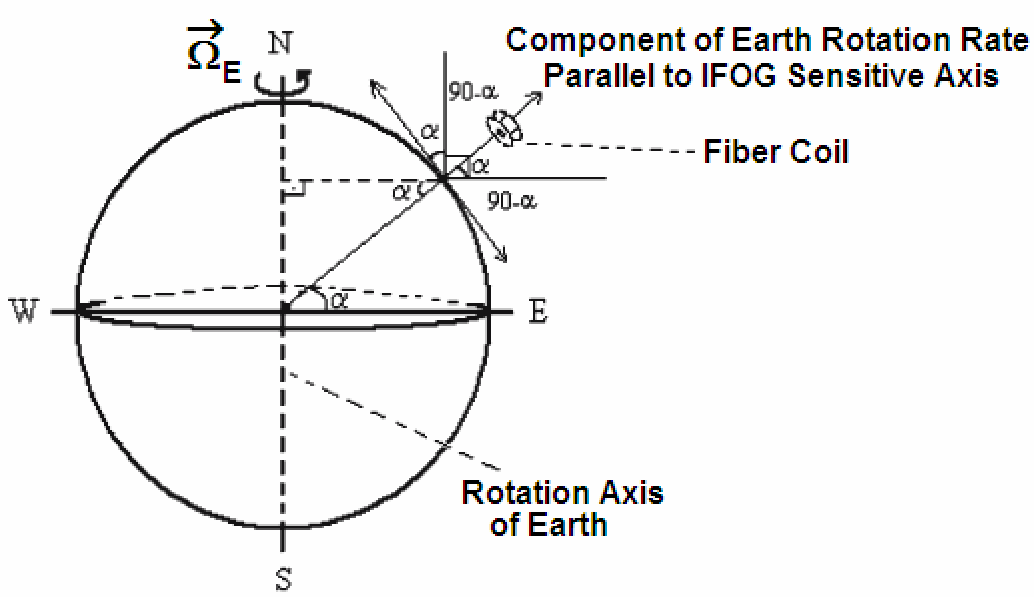

Figure 4.10: Calculation of component of Earth rotation rate

For a complete calibration a temperature chamber is also required to simulate the environmental effects. Turning head of the rate table is coupled inside the temperature chamber and the sensor is mounted inside. And all the tests are conducted while all temperature range is swept. The results are analyzed and the calibration constants are calculated with error analysis. This type of a temperature chamber is shown in figure 4.11.

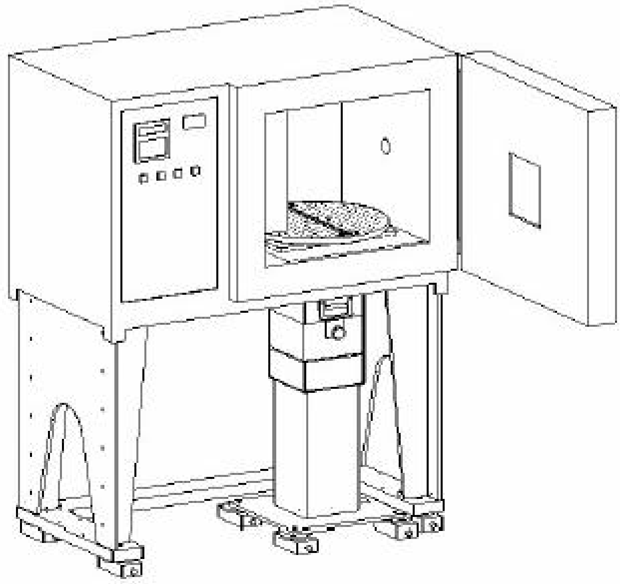

Figure 4.11: Temperature chamber with rate table installed

4.3.1 An Alternative Calibration Method

Without a rate table there is no means to calibrate a gyroscope. At the time our prototypes are built, our rate table was still being shipped. So we designed, developed and constructed a limited precision rate table prototype in range of our capabilities as shown in figure 4.12. For calibration purposes a servo motor is coupled to this rate table.

Figure 4.12: Our rate table prototype

To calibrate the constructed fiber optic gyroscope a calibration procedure, shown in figure 4.13, is designed. In this procedure, a precision reference gyroscope instead of a precision rate table is going to be used along with a data acquisition card. The reference gyroscope has digital output over asynchronous serial interface so its output protocol is decoded and converted to analog or digital parallel signal by a microcontroller card. A special firmware is developed for this microcontroller. Then all analog signals from prototype interferometric fiber optic gyroscope and reference gyroscope are digitized with the aid of data acquisition card. All these data with optical components characterization information will be analyzed with MATLAB and the calibration constants will be obtained for loading into the DSP firmware of the interferometric fiber optic gyroscope.

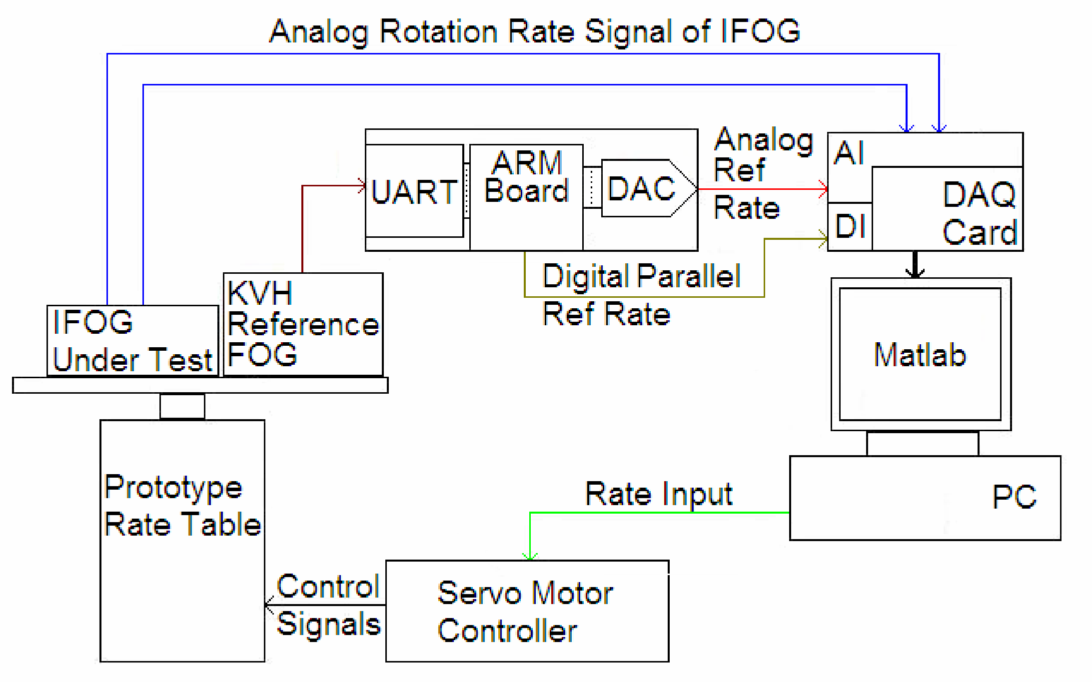

Figure 4.13: IFOG calibration procedure without precision rate table

During mechanical coupling of our prototype rate table with servo motor, calibration grade precision rate table arrived. Due to limited time, we decided to continue the calibration process of prototype IFOGs with that table. Also maximum data output rate of the reference gyroscope is 10 Hz, which is not enough for the dynamic tests.

4.3.2 Calibration with Precision Rate Table

Calibration with precision rate table is performed, closely as possible, according to the related IEEE standards [22,23,24]. Used rate table has an accuracy of 0.01%, which is very good for calibration purposes. The calibration setup used with the precision rate table is shown in figure 4.14.

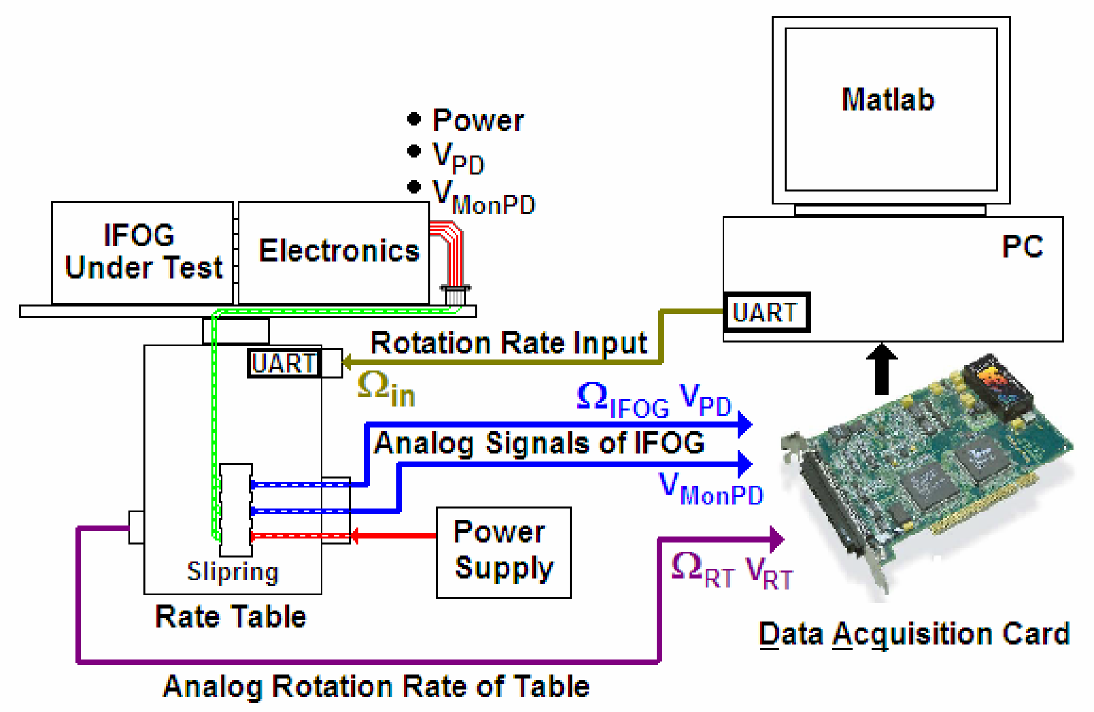

Figure 4.14: IFOG calibration procedure with precision rate table

IFOG and the developed electronics card is mounted on the rate table. Power and amplified analog IFOG signals are connected to the table top connector (red stripped cable in figure). This connector is linked with the connector on the table base via a slip ring mechanism over shielded pair cables inside the rate table. The table base connector is connected to the junction card of the DAQ card (not shown in the figure). This junction card is connected to the DAQ card via an unshielded, 2 m length, 100 pin, parallel ribbon/flat cable. Analog rotation rate signal of the rate table is also connected to this junction card, which is again connected to DAQ card over the same ribbon/flat cable as can be seen in figure 4.8.

The rate table is controlled by a special/proprietary command set developed by the manufacturer of the rate table. These commands are sent to the rate table from PC over UART by means of serial data communication. DAQ card is used to capture analog signals at 1000 Hz data rate.

Calibration of the developed interferometric fiber optic gyroscopes is done by the application of two types of tests: “gyro scale factor tests” and “drift rate tests”. [22] Purposes of gyro scale factor tests are measurement of the scale factor, the scale factor errors and sensitivities. This test is done by the application of a specified rate profile. Purpose of the drift rate tests is measurement of bias, random drift rate, noise and environmental sensitivities. This test is done in a static position for quite a long time. Testing the IFOG prototypes for sensitivity to environmental changes is not possible since there is no temperature chamber available to make these tests.

Rate profile applied for the calibration of the first IFOG is shown in figure 4.15.

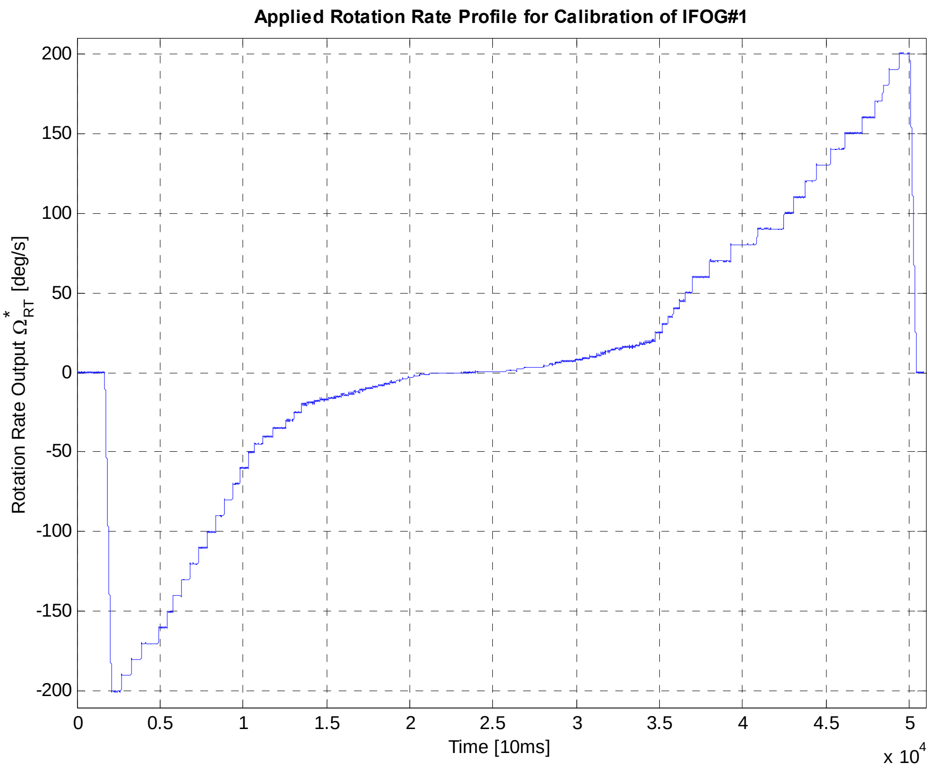

Figure 4.15: Rotation rate profile applied to the IFOG#1

Analog rotation rate output signal, V_{RT} of the rate table is in ±10 V range. A scaling factor SF_{RT} in ${}^{(\deg/s)}\!/_{V}$ units is entered from PC to adjust the corresponding rotation rate. So the rotation rate of the table can be calculated with the following formula;

$$\Omega_{RT} = V_{RT} \cdot SF_{RT} \qquad \textbf{(4.2)}$$

But, before calibration of prototype IFOGs, analog rotation rate output signal of the rate table should be calibrated, too. Value of SF_{RT} was set to 20.6 corresponding to ±206 deg/s from equation 4.2. Real rotation rate of the table is accepted to be very close to the rotation rate entered from PC owing to 0.01% accuracy of the table. To calibrate the rate table a rate profile like in figure 4.15 is applied and analyzed for bias/offset and scale factor errors. After calculation of the corrected scale factor SF^*_{RT} and the bias value V_{BIAS_RT}, corrected rotation rate can be easily obtained with the following equation;

$$\Omega^*_{RT} = (V_{RT} - V_{BIAS\_RT}) \cdot SF^*_{RT} \qquad \textbf{(4.3)}$$

These corrected rate table parameters are used to calculate rotation rate of the table through out the calibration process of IFOG prototypes.

Due to the dynamic properties of the rate table there is a short settling region on every step in a profile like in figure 4.15. These settling regions of the steps are skipped and the average of the remaining part of the step is used for calculation.

4.4 Results

Raw output of the first IFOG prototype is shown in figure 4.16. This graph is plotted using the data from the profile shown in figure 4.15 of corrected rotation rate Ω^*_{RT} of rate table against voltage output V_{IFOG} of the first IFOG prototype.

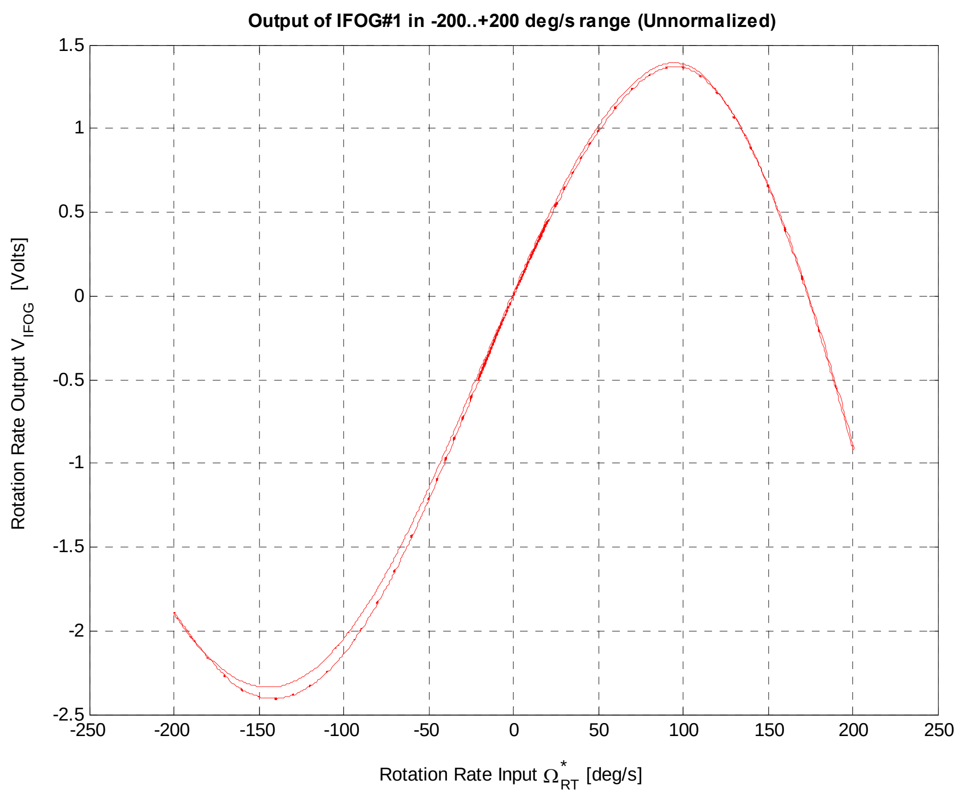

Figure 4.16: Un-normalized output of the first IFOG prototype

As seen in figure 4.16 there is a hysteresis in IFOG output. This hysteresis is due to several factors. Some of the factors contributing this error are thermal effects, light source intensity and wavelength variations. Errors caused by light source intensity variations can be easily compensated by normalizing the output of IFOG by the measured light source intensity via a monitor photodiode. Normally output of IFOG is calculated with equation 4.4;

$$V_{IFOG} = V_{PD} - V_{BIAS\_IFOG} \tag{4.4}$$

where V_{PD} is raw voltage output of the photo diode and V_{BIAS_IFOG} is the value of V_{PD} when there is no rotation. Normalization is done according to the equation 4.5;

$$V^{*}_{IFOG} = V_{PD} / V_{MonPD} - V_{BIAS\_IFOG} \tag{4.5}$$

where V_{MonPD} is the voltage output of monitor photo diode measuring intensity of the light source. Normalized output of first IFOG is shown in figure 4.17.

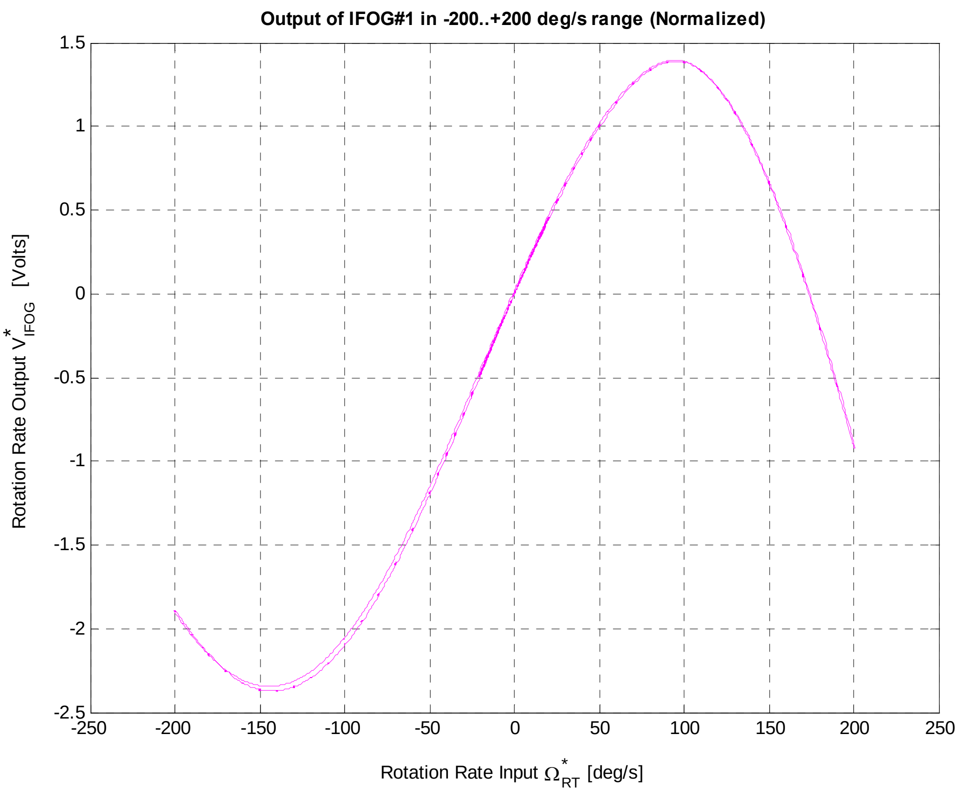

Figure 4.17: Normalized output of the first IFOG prototype

Normalization lessens the hysteresis of the output of gyro which can be seen by comparing figures 4.16 and 4.17.

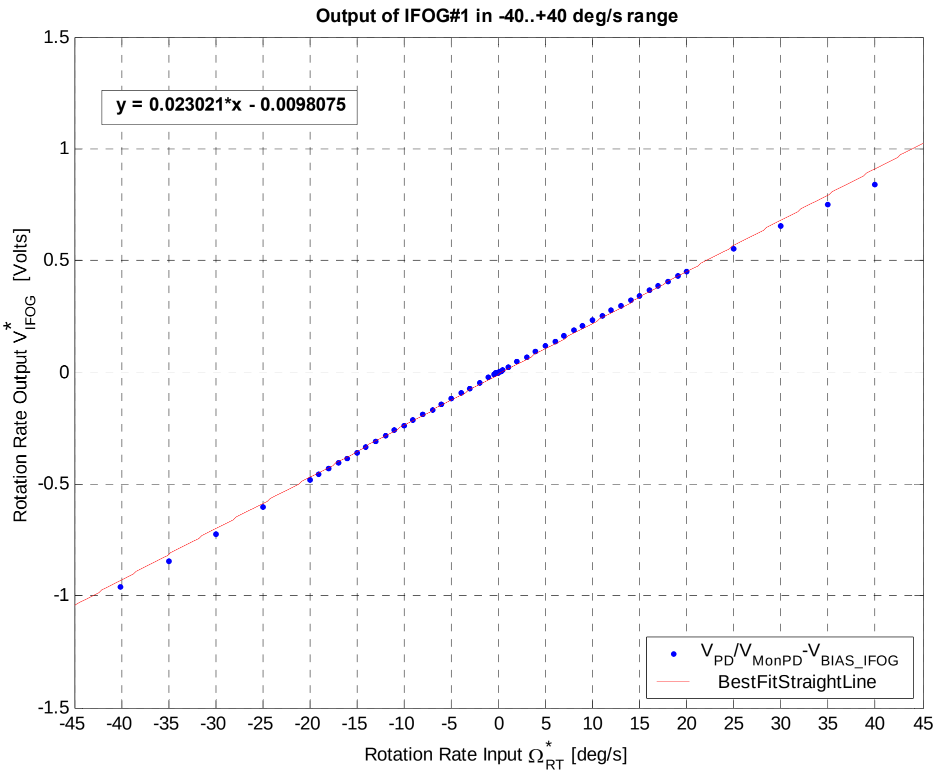

Figure 4.18: Scale factor of first IFOG

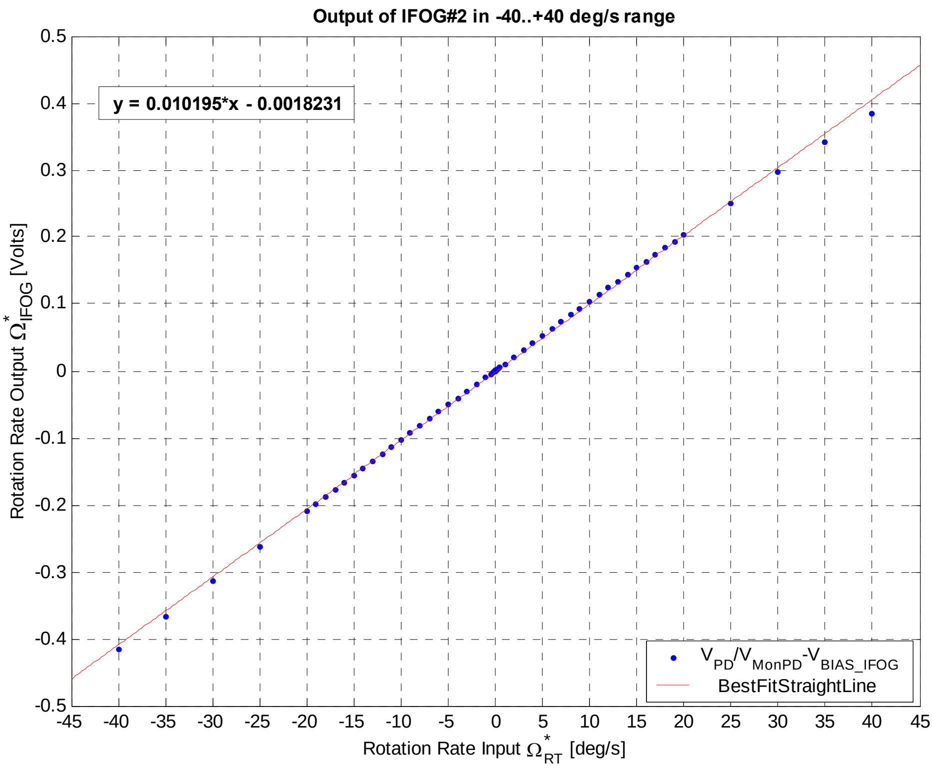

Figure 4.19: Scale factor of second IFOG

In the first stage of the calibration, "gyro scale factor tests" are carried out. Scale factor SF_{IFOG} of prototype interferometric fiber optic gyroscope is calculated by fitting a straight line to the normalized IFOG output V^*_{IFOG} data in range ±40 degrees per second by least-squares method. This fit is called Best Fit Straight Line, BFSL which is shown in figures 4.18 and 4.19. The equations of the BFSLs are written on the plots. The coefficient of x gives us the scale factor, SF_{IFOG} in $V/(\frac{\deg}{s})$ units. Then, dividing V^*_{IFOG} by this scale factor the sensor output Ω^*_{IFOG} is obtained in deg/s. Equation 4.6 shows the calculation of sensed rotation rate by IFOG;

$$\Omega^*_{IFOG} = V^*_{IFOG} / SF_{IFOG} \tag{4.6}$$

Figures 4.20 and 4.21 shows the scale factor nonlinearities for the calculated scale factors concerning the first and the second IFOG respectively.

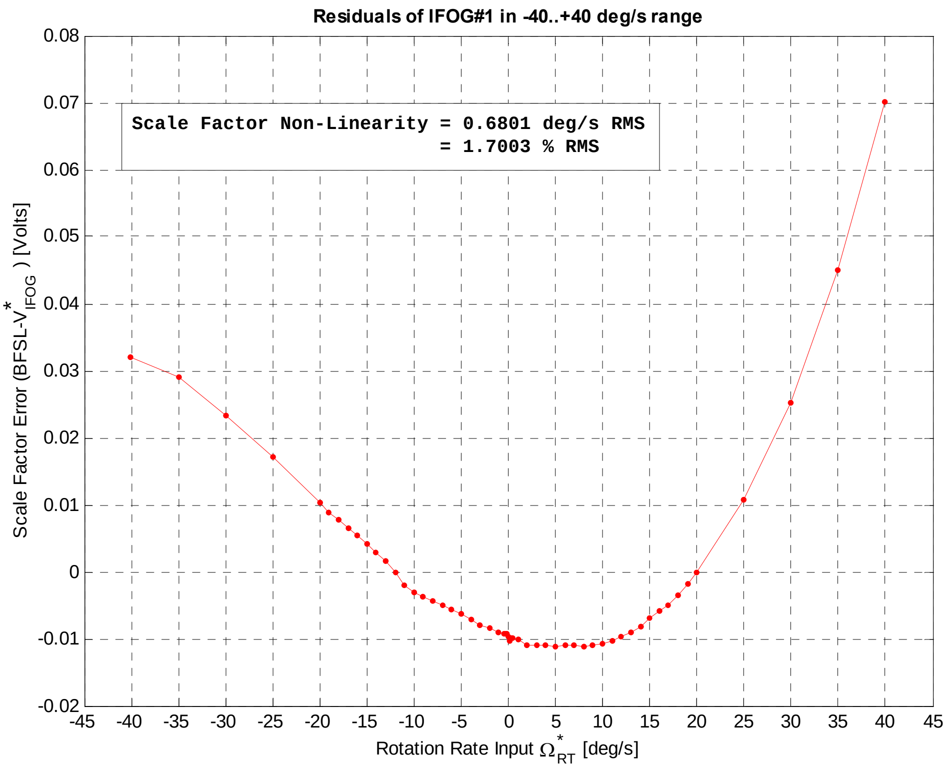

Figure 4.20: Scale Factor Nonlinearity of the first IFOG

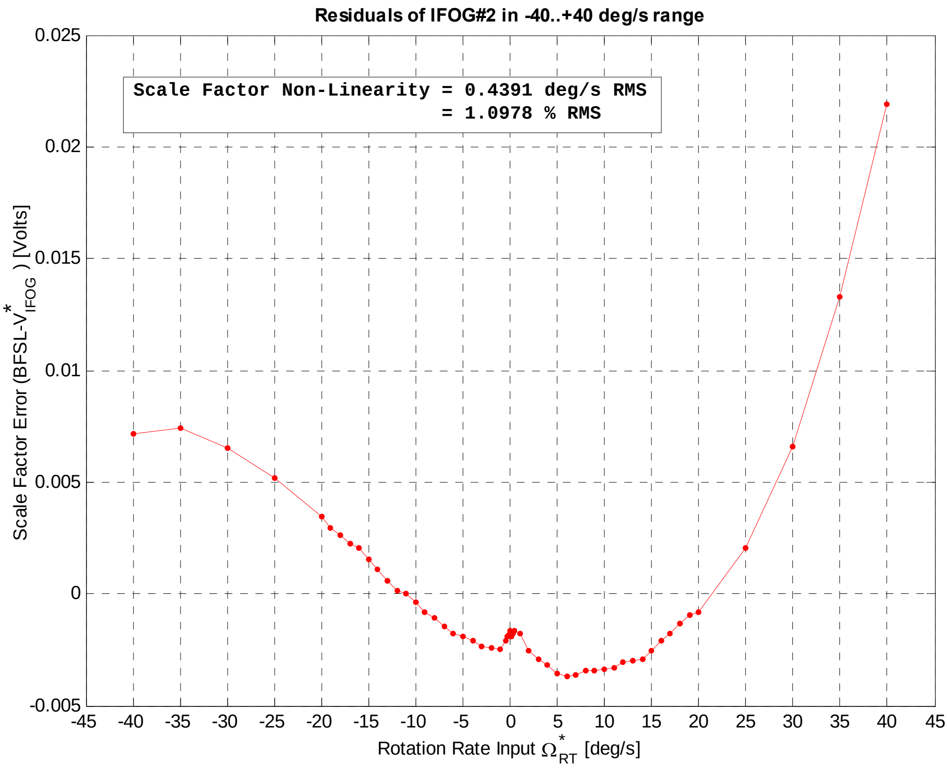

Figure 4.21: Scale Factor Nonlinearity of the second IFOG

Nonlinearity of the scale factor is calculated by subtracting the ordinates of the real gyro output V^*_{IFOG} from Best Fit Straight Line, giving the residuals. This is shown in figures 4.20 and 4.21 for first and second IFOG respectively. Root-Mean-Square of these residuals is calculated and divided by the scale factor to get RMS scale factor error in degrees per second units.

After the scale factor SF_{IFOG} is calculated IFOG output V^*_{IFOG} can be plotted as degrees per second units according to the equation 4.6 which is shown in figures 4.22 and 4.23 for the first and second IFOG respectively. According to the Best Fit Straight Line equation slope is 1 which is the ideal sensor output. But because of the nonlinearity whose value is calculated before, some points do not coincide exactly with the Best Fit Straight Line. The residuals of difference are shown in figures 4.24 and 4.25. This again gives the same nonlinearity results.

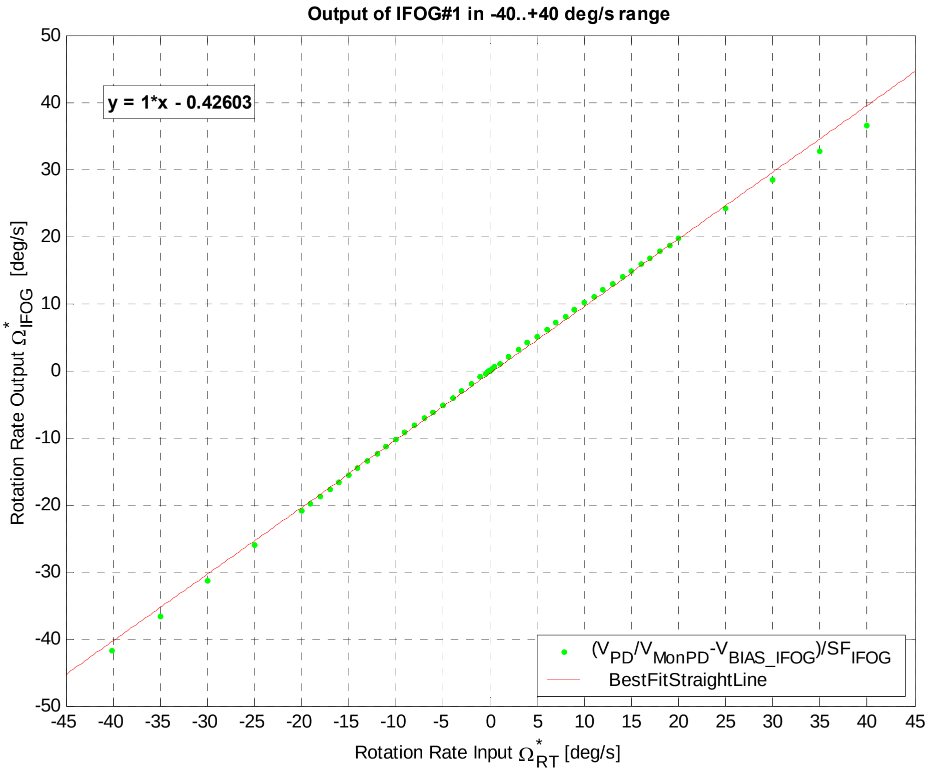

Figure 4.22: Scale Factor of the first IFOG

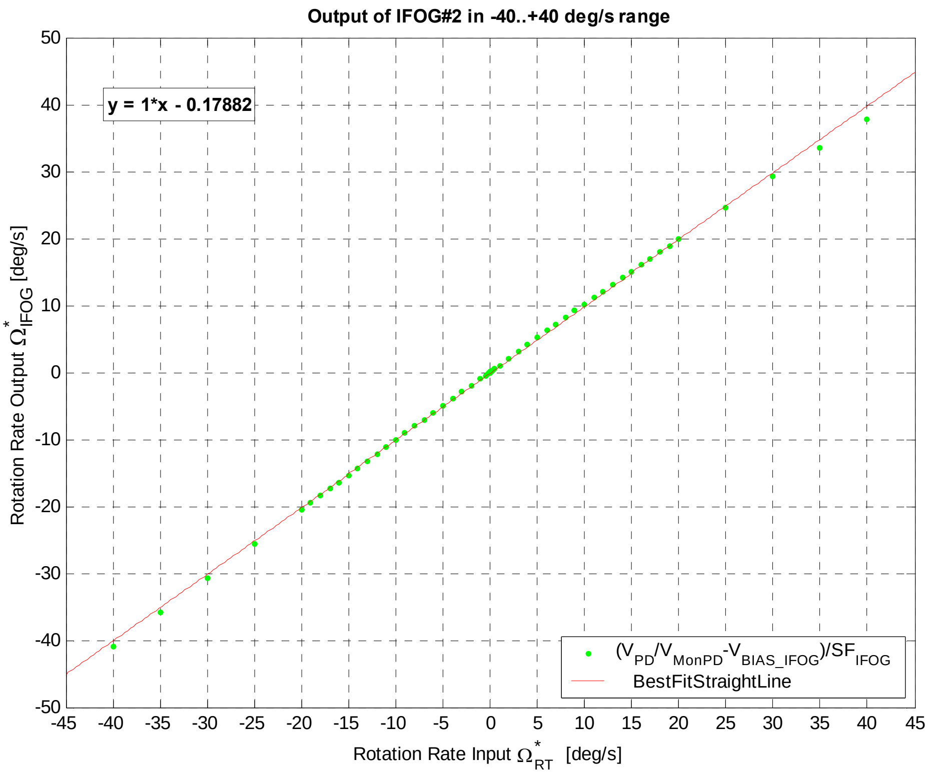

Figure 4.23: Scale Factor of the second IFOG

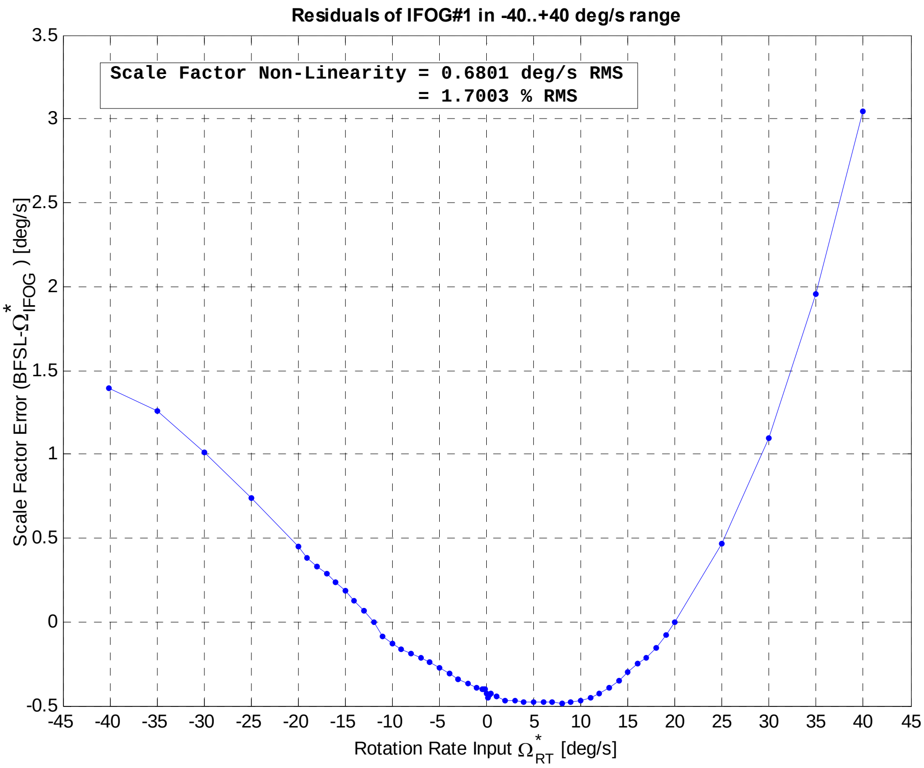

Figure 4.24: Scale Factor Nonlinearity of the first IFOG

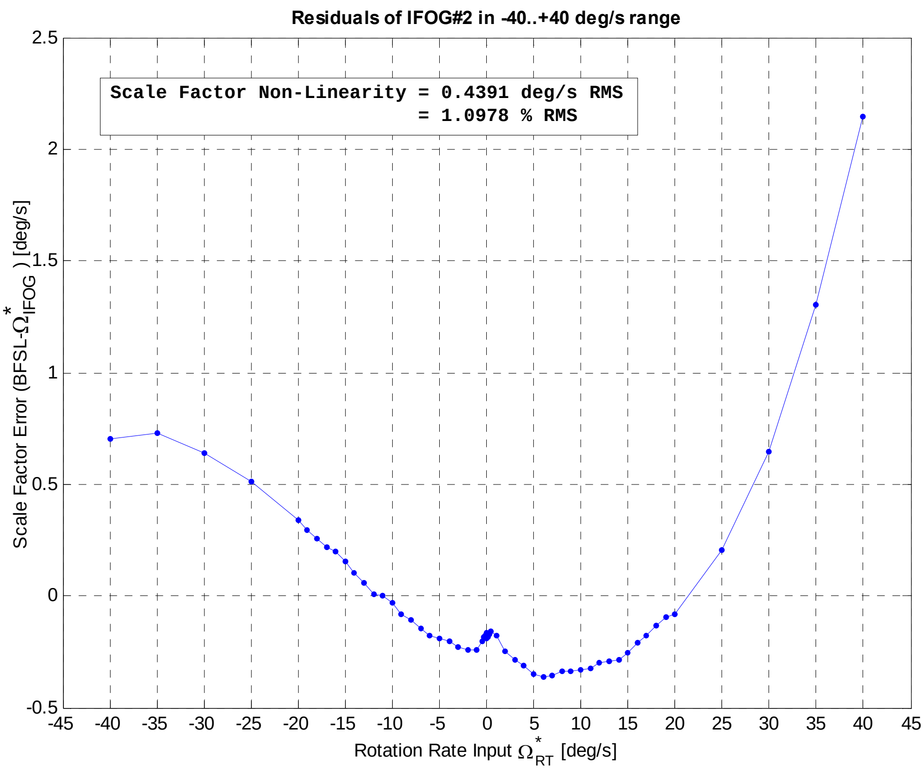

Figure 4.25: Scale Factor Nonlinearity of the second IFOG

Second stage of the calibration is "drift rate testing" of the interferometric fiber optic gyroscopes. In this stage IFOG is held motionless. And, output of IFOG V_{IFOG}^{*} is recorded for a long time which is related with the application's mission time.

As shown in figures 4.26 and 4.27, bias plots of IFOG prototypes, are recorded for 20 minutes which is enough for short range and dead-reckoning applications.

This data is processed to find the peak-to-peak deviation and standard deviation. The calculated values are shown in the figures.

The reason for the high noise on IFOG output is due to coupled electrical noise from the environment. This noise is coupled mainly from the long and unshielded DAQ flat cable. Long signal path going through a slip ring stretching from IFOG to the DAQ card is also a contributor of the coupling noise. These can be overcome by integrating all the signal processing into IFOG electronics, which will be the next step of the design. Frequency domain analysis of the IFOGs bias signals indicate peaks around 250 and 450Hz which may be harmonics of the power supply source. Switch mode power supply of the DAQ PC is also a source of the electrical noise.

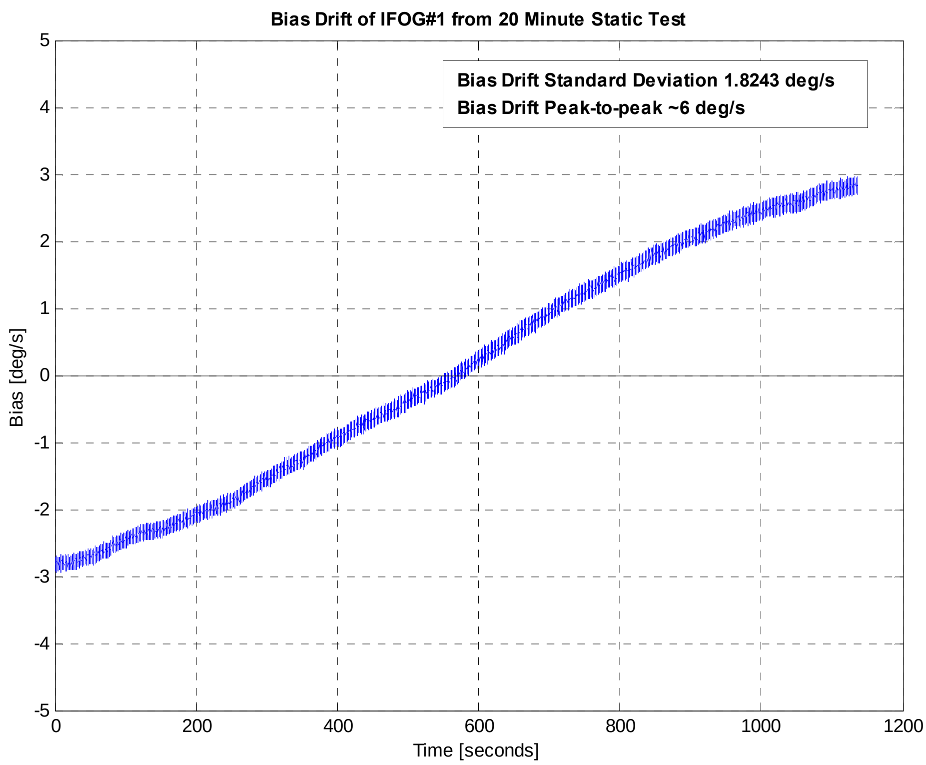

Figure 4.26: Bias Drift of the first IFOG

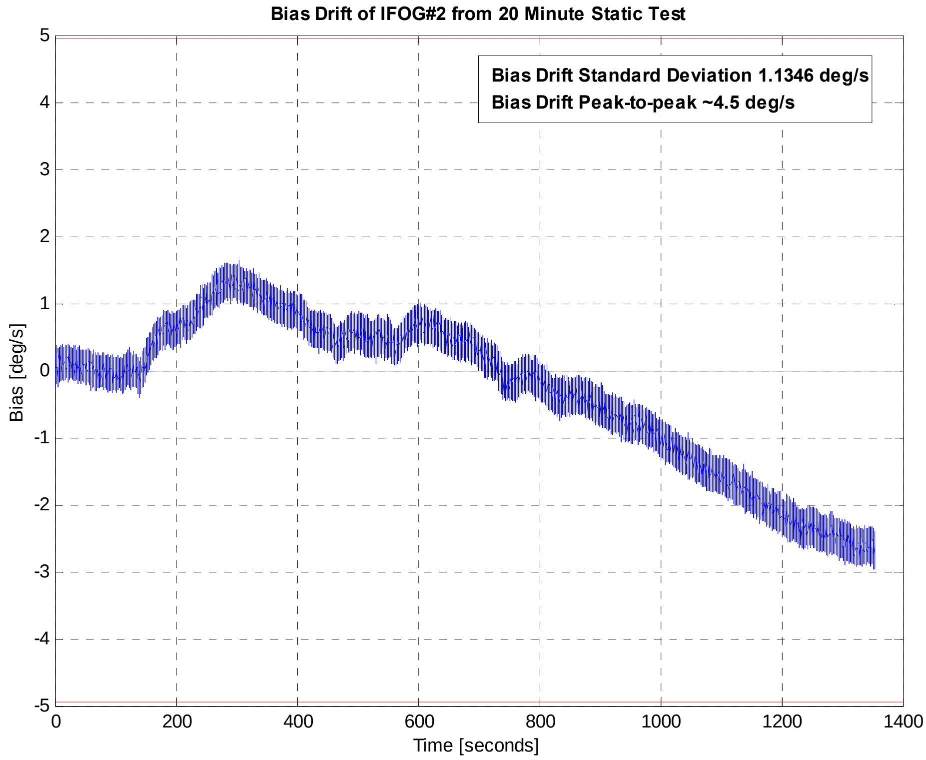

Figure 4.27: Bias Drift of the second IFOG

Noise calculation of the gyroscopes is done by Allan Variance Analysis. The calculation is done on the data shown in figure 4.26 and 4.27 according to IEEE Standards [22,25]. Allan Variance formulation is given in equation 4.7.

$$AVAR^2(\tau) = \frac{1}{2\cdot(n-1)}\sum_{i=1}^{n-1}\left[y(\tau)_{i+1} - y(\tau)_i\right]^2 \qquad \textbf{(4.7)}$$

where $AVAR^2(\tau)$ is the Allan Variance as a function of the averaging time/time constant τ, $y(\tau)_i$ is the average value of the measurement bin *i* and *n* is the total number of bins.

Sampling rate of the bias data is chosen as 1000 Hz which is equivalent to 1 ms sampling period. So, minimum time constant for Allan Variance calculation is chosen as 10 milliseconds, corresponding to 10 data points for averaging. The other time constants were chosen to form the slope of -1/2 of $\log_{10}/\log_{10}$ plot which is used to calculate the Angle Random Walk. Figure 4.28 and 4.29 shows the result of Allan Variance calculations with Angle Random Walk and maximum achievable Bias Stability values.

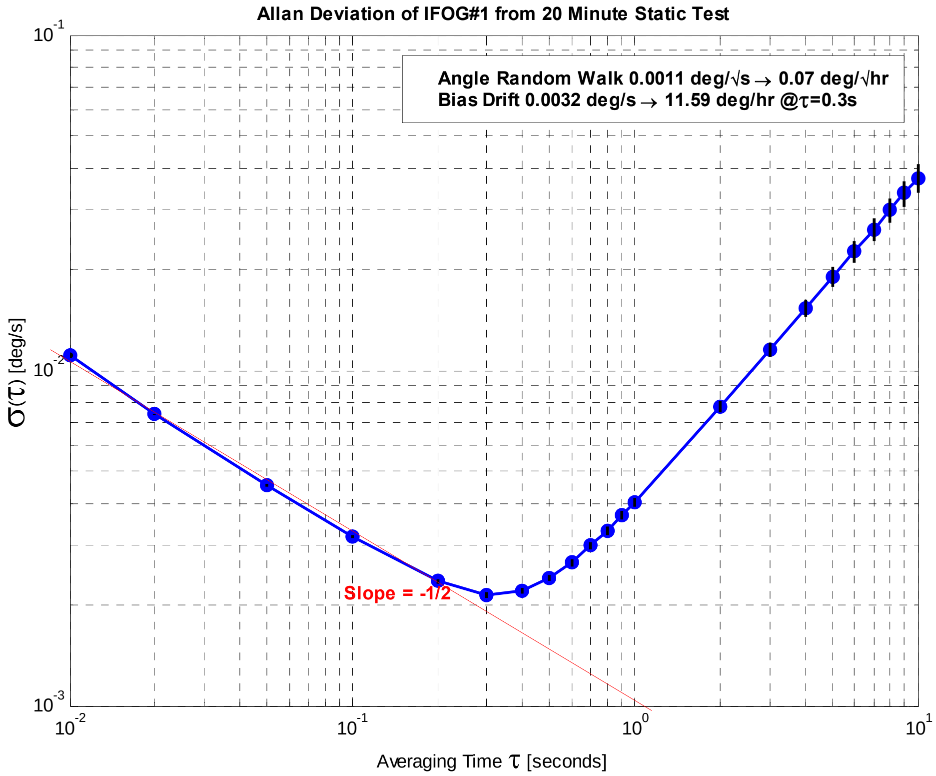

Figure 4.28: Allan Deviation of the first IFOG

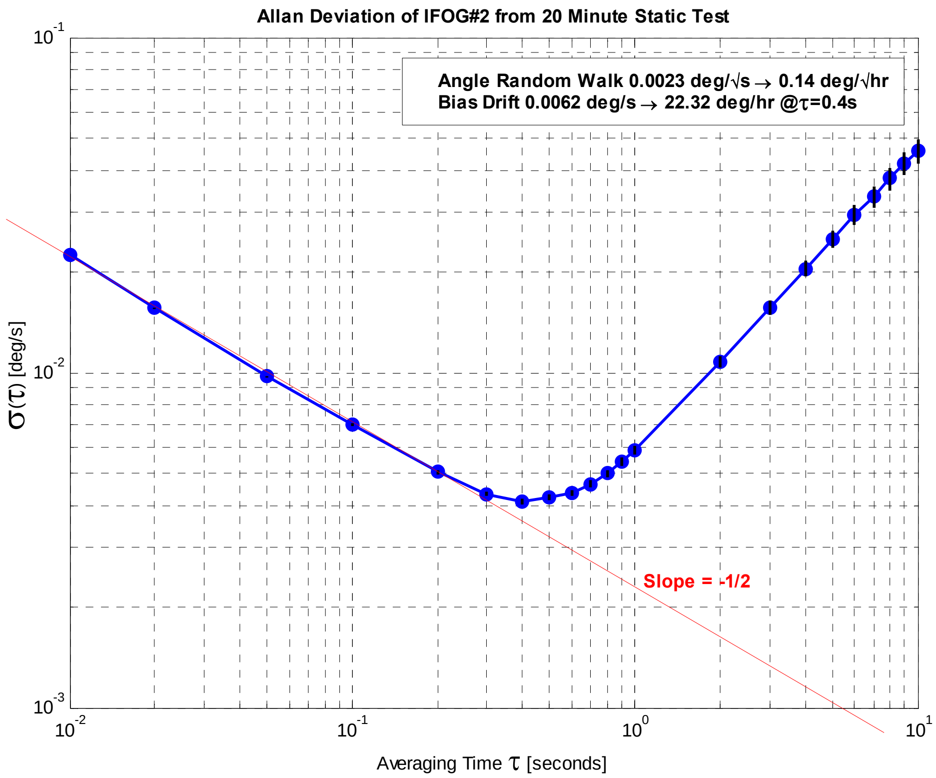

Figure 4.29: Allan Deviation of the second IFOG

Figure 4.30 is the proof of 0.05 deg/s resolution of the IFOG prototype. The small table inside the plot shows averages of the steps for Ω_{in}, Ω^*_{RT}, Ω^*_{IFOG} data. Drift on the steps is due to thermal effects of the environment since there is no temperature control or stabilization.

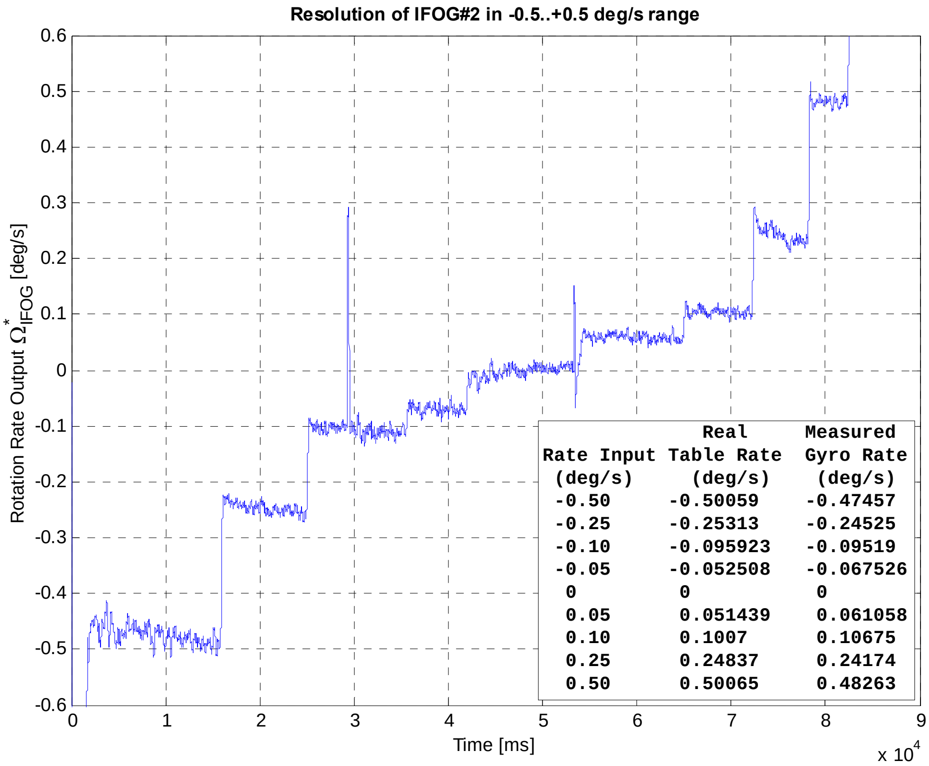

Rate Input (deg/s)	Real Table Rate (deg/s)	Measured Gyro Rate (deg/s)
-0.50	-0.50059	-0.47457
-0.25	-0.25313	-0.24525
-0.10	-0.095923	-0.09519
-0.05	-0.052508	-0.067526
0	0	0
0.05	0.051439	0.061058
0.10	0.1007	0.10675
0.25	0.24837	0.24174
0.50	0.50065	0.48263

Figure 4.30: Resolution of second IFOG

In figures 4.31, 4.32 and 4.33 the performance of the developed IFOGs are demonstrated after calibration. For higher rotation rates increasing nonlinearity is clearly seen in figure 4.31. But in working range of ±40 deg/s, IFOG output follows rotation rate of table closely. This can be seen by inspecting the minimal variations in figure 4.31.

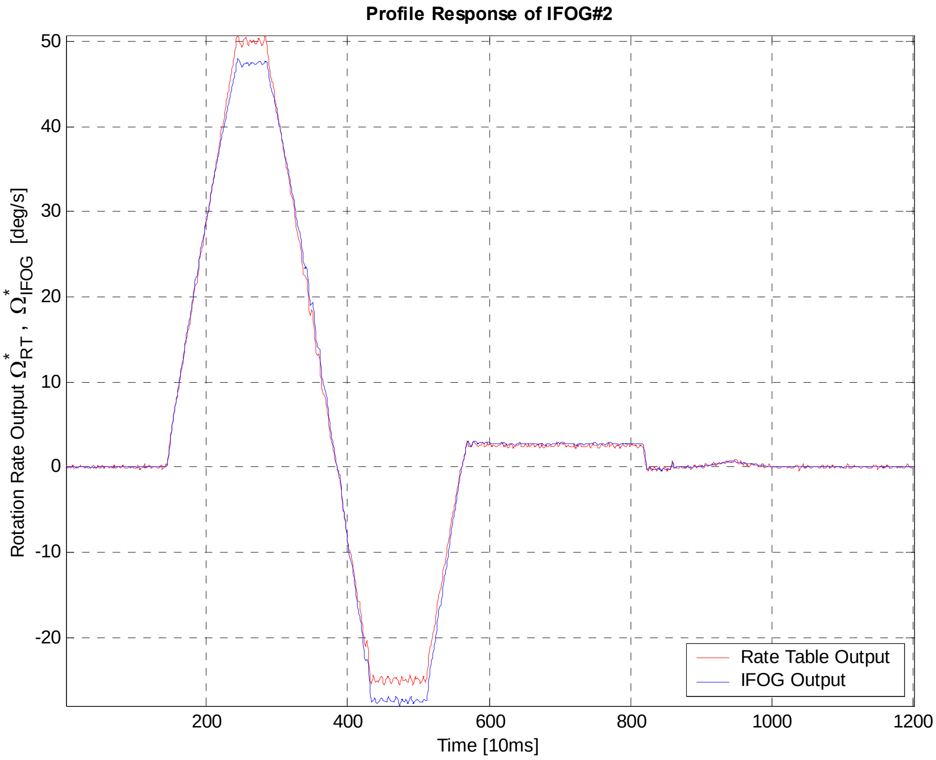

Figure 4.31: Performance of the second IFOG

In figure 4.32 and 4.33 sinusoidal rotation rate is applied to the IFOG prototypes. Careful inspection of both figures reveals that IFOG outputs follows every single curl and twist closely. In figure 4.33, IFOG output following the rate table's dynamics while stopping is observed as well.

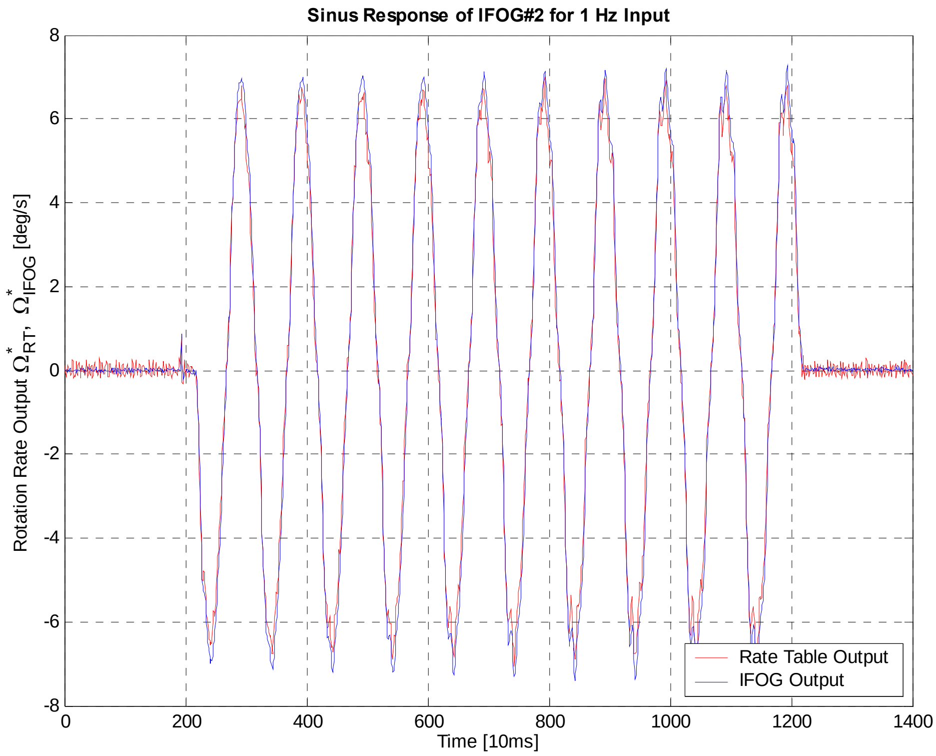

Figure 4.32: Performance of the second IFOG for 1Hz Sinusoidal Rotation

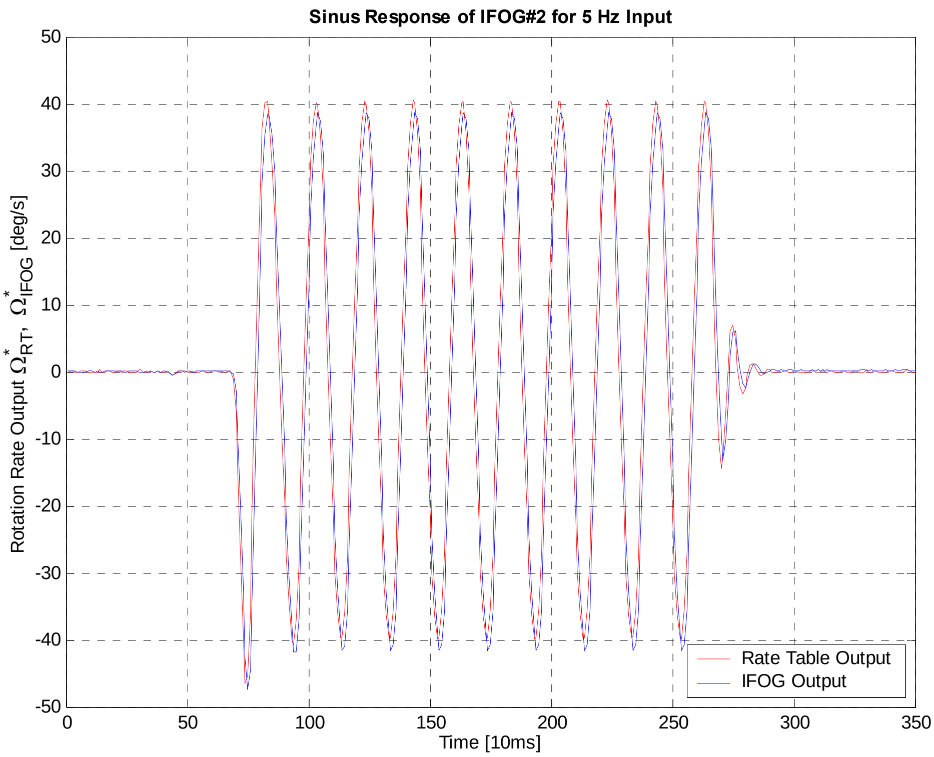

Figure 4.33: Performance of the second IFOG for 5Hz Sinusoidal Rotation

All results collected during calibration tests are compiled into table 4.2. According to the calibration tests both IFOGs demonstrated similar performance. This proves the repetability of the IFOG construction.

Table 4.2: Consolidated calibration results of the IFOG prototypes

	IFOG#1	IFOG#2	Units	Source
Optical Scale Factor	0.7667	0.7662	rad/(deg/s)	Nominal Value = 0.71s
Electrical Scale Factor	0.023021	0.010195	mV/(deg/s)	Best Fit Straight Line
Scale Factor Error	0.68	0.44	deg/s RMS	Residuals
(Non-Linearity)	1.7	1.09	% RMS	
Bias Stability	0.0032	0.0062	deg/s	Allan Deviation
(UnFiltered)	11.59	22.32	deg/h	Allan Deviation
	1.82	1.13	deg/s	Std Dev
	~6	~4.5	deg/s	Peak-to-Peak
Angle Random Walk	0.0011	0.0023	deg/sqrt(s)	Allan Deviation
(Unfiltered)	0.07	0.14	deg/sqrt(h)	Allan Deviation
Output Optical Power	~1.1	~0.9	uW	Measurements
Noise Equivalent Rate	~0.0016	~0.0018	deg/s	Photon Shot Noise@τ=10 ms

Experimentally measured optical scale factor values are in accord with the theoretical values. Little difference is caused by thermal expansion of the optical fiber leading to increased area of the sensing loop.

5. CONCLUSION

Two working prototype interferometric fiber optic gyroscopes of minimum 0.05 degree per second resolution are developed in laboratory.

Low power consumption of developed IFOG prototypes makes them suitable for mobile applications.

Developed IFOGs could be easily packaged into a 10x10x10 centimeter cube without miniaturization, which is useable in robotics and stabilization applications.

With proper temperature control, model based compensation and packaging, resolution and stability would be enhanced at least one order of magnitude which is useable for short range tactical applications, robotics, dead reckoning and platform stabilization applications.

REFERENCES

[1] **Sagnac effect**, http://en.wikipedia.org/wiki/Sagnac_effect, Wikipedia

[2] **The Sagnac Effect**, http://www.mathpages.com/rr/s2-07/2-07.htm

[3] **Georges Sagnac**, http://en.wikipedia.org/wiki/Georges_Sagnac, Wikipedia

[4] **Sagnac Interferometer**, http://www.physik.fu-berlin.de/~bauer/habil_online /node11.html

[5] **Rodloff, R.**, 1999, Physical Background and Technical Realization, *Optical Gyros and Their Applications, RTO-AG-339*, 2-1 – 2-16.

[6] **Bergh, Ralph A., Lefevre, H.C. and Shaw, Herbert J.**, 1984, An Overview of Fiber-Optic Gyroscopes, *IEEE Journal of Lightwave Technology*, **2** No.2, 91-107.

[7] **Leferve, Herve C.**, 1999, Application of the Sagnac Effect in the Interferometric Fiber-Optic Gyroscope, *Optical Gyros and Applications*, *RTO-AG-339*, 7-1 – 7-29.

[8] **Arditty, H.J. and Lefevre, H.C.**, 1981, Sagnac effect in fiber gyroscopes, *OSA Optics Letters*, **6**(8), 401-403.

[9] **Ezekiel, S. and Arditty, H.J.**, 1982, Fiber-Optic Rotation Sensors, Springer-Verlag Heidelberg, Fiber-Optic Rotation Sensors and Related Technologies, 2-26.

[10] **Burns, William K.**, 1994, Optical Fiber Rotation Sensing, Academic Press, Boston.

[11] **Lefevre, H.C.**, 1993, The Fiber-Optic Gyroscope, Artech House, Boston.

[12] **Post, E.J.**, 1967, Sagnac Effect, *Rev.Mod.Phys.*, **39**, 475-494.

[13] **Giallorenzi, T.G.**,1986, Progress in Optical Fiber Sensors, *AGARD-CP-383*, 1-1 – 1-13.

[14] **Hecht, Eugene,** 1998, Optics, Addison Wesley, 3rd Ed.

[15] **Feynman, R.P., Leighton, R.B.,Sands M.,** 1977, Lectures on Physics, Addison Wesley.

[16] **Culshaw, Brian, Dakin, John,** 1989, Optical Fiber Sensors: Systems and Applications, Vol II Artech House, Norwood

[17] **Faraday Effect,** http://en.wikipedia.org/wiki/Faraday_effect, Wikipedia

[18] **Kerr Effect**, http://en.wikipedia.org/wiki/Kerr_effect, Wikipedia

[19] **Shupe, D.M.**, 1980, Thermally induced nonreciprocity in the fiber-optic interferometer, *OSA Applied Optics*, **19**(5), 654-655.

[20] **Sammarco, J.J.**, 1990, Mining Machine Orientation Control Based on Inertial, Gravitational, and Magnetic Sensors, Report of Investigations 9326, US Bureau of Mines, Pittsburgh, PA.

[21] **Culshaw, Brian**, 2006, The optical fibre Sagnac interferometer: an overview of its principles and applications, *Meas. Sci. Technol.*, **17**, R1–R16.

[22] **IEEE Std 952-1997**, 1998, IEEE Standard Specification Format Guide and Test Procedure for Single-Axis Interferometric Fiber Optic Gyros, IEEE Standards, New York, USA.

[23] **IEEE Std 1554-2005**, 2005, IEEE Recommended Practice for Inertial Sensor Test Equipment, Instrumentation, Data Acquisition, and Analysis, IEEE Standards, New York, USA.

[24] **IEEE Std 528-2001**, 2001, IEEE Standard for Inertial Sensor Terminology, IEEE Standards, New York, USA.

[25] **Stockwell, Walter**, 1998, Bias Stability Measurement: Allan Variance, Crossbow Technology, Inc, San Jose, USA.

BIOGRAPHY

İsmet Faik SAĞLAR was born in 1976 in İstanbul. He graduated from F.M.V Özel Işık Lisesi in 1994 and started İ.T.Ü Control and Computer Engineering same year. In 1998, he started his professional business life. In 2000, he graduated from İ.T.Ü Control and Computer Engineering earning B.Sc. degree. He started İ.T.Ü Control and Automation Engineering master programme in 2002. He completed his military service at Turkish General Staff – Smart Card Management Center with title Personalization Officer between December 2004 and October 2005. He worked for several technology companies including freelance consulting on embedded systems projects starting from 1998.